

# Reheating and magma mixing recorded by zircon and quartz from high-silica rhyolite in the Coqen region, southern Tibet

(Reversion 1)

Shao-Rong Chen<sup>1</sup>, Qing Wang<sup>1\*</sup>, Di-Cheng Zhu<sup>1</sup>, Roberto F. Weinberg<sup>2</sup>, Liang-Liang  
Zhang<sup>1</sup>, Zhi-Dan Zhao<sup>1</sup>

1 State Key Laboratory of Geological Processes and Mineral Resources, and School of  
Earth Science and Resources, China University of Geosciences, Beijing 100083, China  
2 School of Earth, Atmosphere and Environment, Monash University, Melbourne, VIC  
3800, Australia

Manuscript resubmitted (May 12<sup>nd</sup>, 2020) to [American Mineralogist](#)

\*Corresponding author: **Qing Wang**

State Key Laboratory of Geological Processes and Mineral Resources  
China University of Geosciences  
29# Xue-Yuan Road, Haidian District  
Beijing 100083, China  
Phone: (+86) 010 8232 2094 (O)  
Fax: (+86) 010 8232 2094  
Email: [qing726@126.com](mailto:qing726@126.com)

## Abstract

Understanding the formation of high-silica rhyolites (HSRs,  $\text{SiO}_2 > 75 \text{ wt\%}$ ) is critical to reveal the evolution of felsic magma systems and magma chamber processes. This paper addresses HSR petrogenesis by investigating an integrated dataset of whole-rock geochemistry, geochronology and mineral composition of the ~74 Ma Nuocang HSR ( $\text{SiO}_2 = 74.5\text{--}79.3 \text{ wt\%}$ ) from the Coqen region in southern Tibet. Cathodoluminescence (CL) images show that zircons from the Nuocang HSRs can be divided into two textural types: those with dark-CL cores displaying resorption features and overgrown by light-CL rims, and those comprising a single light-CL zone, without dark-CL cores. In situ single-spot data and scanning images demonstrate that these two types of zircon have similar U–Pb ages (~74 Ma) and Hf isotopic compositions ( $\epsilon_{\text{Hf}}(t) = -9.09$  to  $-5.39$ ), indicating they were generated by the same magmatic system. However, they have different abundances of trace elements and trace element ratios. The dark-CL cores are likely crystallized from a highly evolved magma as indicated by their higher U, Th, Hf, Y, and heavy rare earth elements concentrations, lower Sm/Yb ratio and more negative Eu anomalies. In contrast, the uniformly light-CL zircons and the light-CL rims are likely crystallized from less evolved and hotter magma, as indicated by their lower U–Th–REE abundances and higher Ti-in-zircon temperatures. This is consistent with the Ti-in-quartz geothermometer in quartz phenocrysts which reveals that the light-CL zones are hotter than dark-CL cores. We propose that the composition and temperature differences between cores and rims of zircons and quartz record a recharge and reheating event during the formation of the Nuocang HSRs. This implies that HSR is a result of mixing between a hotter, less evolved silicic magma and a cooler, highly evolved and

47 crystal-rich mush. This paper shows that zircon and quartz with distinct internal textures  
48 can be combined to disentangle the multi-stage evolution of magma reservoirs, providing  
49 critical insights into the origin of HSRs.

50 **Keywords:** high-silica rhyolites, zircon trace elements, Ti-in-quartz geothermometer,  
51 magmatic process, Lhasa Terrane

52

53

## Introduction

High-silica rhyolites (HSRs) (e.g.,  $\text{SiO}_2 > 75$  wt%, [Gualda and Ghiorso, 2013](#)) are an important component of the upper continental crust. Determining the magmatic processes involved in the formation of HSRs is critical to understanding the evolution of felsic magmas. Both the extended fractional crystallization of low-silica magmas ([Bachmann and Bergantz, 2008](#); [Nandedkar et al., 2014](#); [Lee and Morton, 2015](#)) and the low-degree partial melting of source materials ([Streck, 2002](#); [Sisson et al., 2005](#); [Simakin and Bindeman, 2012](#)) can generate high-silica magmas directly. Discriminating the two mechanisms using whole-rock geochemistry only is difficult because they have similar compositional effects (e.g., [Moyen et al., 2017](#); [Tang et al., 2019](#)). Furthermore, it is not always possible to recognize the superposition of multiple processes in magma evolution using whole-rock geochemistry of sample suites only (e.g., [Keller et al., 2015](#); [Gao et al., 2016](#)).

Zircons are refractory accessory minerals that once formed tend to preserve their chemical and isotopic nature. Thus, zircon U–Pb age, trace element, and Hf–O isotopic data can be used to investigate complexities in the evolutionary path of the magmatic rocks hosting them ([Kemp et al., 2007](#); [Yang et al., 2007](#); [Bindeman et al., 2008](#)). This is especially true for zircons with distinct internal textures, which record diverse crystallization conditions and thus provide direct lines of evidence for complex crystallization history and magmatic processes ([Claiborne et al., 2010a](#); [Reid et al., 2011](#); [Chamberlain et al., 2014](#); [Matthews et al., 2015](#); [Yan et al., 2018](#)). Likewise, quartz with compositional zones has also been proven to be a powerful proxy to investigate changes of chemistry and temperature conditions in silicic magma chambers ([Wark et al., 2007](#);

Wiebe et al., 2007; Shane et al., 2008; Audétat, 2013). As a result, combining the chemical characterization of zircon and quartz with distinct internal textures is expected to provide information complementary to whole-rock geochemical composition.

In this study, we present the whole-rock major and trace element data, zircon U–Pb ages, and zircon trace elements and Hf–O isotopes of the late Cretaceous Nuocang HSRs in the Coqen region of Tibet, located at the northern margin of southern Lhasa Terrane (Fig. 1a). The data show that different zircon domains yield identical U–Pb age (~74 Ma) within analytical uncertainty, but display substantial differences in elemental concentrations. We combine this information with Ti-in-quartz geothermometer, to propose that the compositional differences between cores and rims of zircons and of quartz phenocrysts record the reheating and magma mixing in a pre-eruptive magma reservoir.

## Geological background and samples

The Tibetan Plateau is a geological collage, which from north to south comprises the Songpan-Ganzi flysch complex zone, Eastern Qiangtang, Western Qiangtang, Lhasa Terrane, and the Himalayas, separated by Jinsha (JSSZ), Longmu Tso-Shuanghu (LSSZ), Bangong-Nujiang (BNSZ), and Indus-Yarlung Zangbo suture zones (IYZSZ) (Fig. 1a), respectively (Zhu et al., 2013). The Lhasa Terrane can be further divided into the northern, central, and southern Lhasa subterrane by the Shiquan River-Nam Tso ophiolitic mélange zone (SNMZ) and the Luobadui-Milashan fault zone (LMF) (Fig. 1a). These three subterrane have differences in the character of the sedimentary cover and nature of

basement rocks (Zhu et al., 2011). The northern Lhasa subterrane consists mainly of Middle Triassic to Cretaceous sedimentary rocks, Lower Cretaceous volcanic rocks and granitoids, and is characterized by juvenile crust (Pan et al., 2004; Zhu et al., 2011). In the central Lhasa subterrane, Archean-Proterozoic crystalline basement is widely overlain by Carboniferous-Permian metasedimentary rocks, Lower Jurassic to Lower Cretaceous sedimentary and volcanic rocks, and intruded by Early Cretaceous granitoids with some Ordovician, Silurian, Devonian, and Triassic limestones (Pan et al., 2004; Zhang et al., 2010; Zhu et al., 2011). The magmatic rocks in the southern Lhasa subterrane are comprised mainly of the Jurassic-Cretaceous Gangdese Batholith and Linzizong volcanic succession. This subterrane is dominated by juvenile crust with Precambrian crystalline basement found locally in the eastern part (Ji et al., 2009; Zhu et al., 2013; Zhang et al., 2020).

This study focuses on the Cretaceous Nuocang rhyolite from the northern margin of the western segment of the southern Lhasa subterrane, ~70 km south of Coqen County (Fig. 1b). Upper Cretaceous volcanic rocks are widely exposed in this area. These rocks overlie sandstones and slates of the Lower Carboniferous Yongzhu Formation, sandstones and limestones of the Lower Permian Angjie Formation, and are intruded by Cenozoic granitoids. The rhyolite samples were collected ~1–2 km southwest of the Nuocang Village (Fig. 1c, d). These rocks were assigned by the geological survey to the Dianzhong Formation of the Paleocene Linzizong volcanic succession [1:250,000 scale map, Coqen regional geological survey report (H45C002001), 2003]. These rhyolites show porphyritic texture with phenocrysts of quartz (~15–20%), K-feldspar (~5–10%) and plagioclase (~5%) (Fig. 1e). Quartz phenocrysts are embayed and display melt inclusions,

irregular open cracks and fractures (Fig. 1f, g), like the volcanic quartz described by Bernet and Bassett (2005). The accessory minerals consist mainly of zircon, apatite, and iron oxides. These volcanic rocks have experienced various degrees of alteration evidenced by kaolinized K-feldspar.

### Analytical methods

Whole-rock major and trace elements were measured at the State Key Laboratory of Geological Processes and Mineral Resources, China University of Geosciences (Wuhan) by X-ray fluorescence and inductively coupled plasma mass spectrometry (ICP-MS), respectively, described in detail by Yang et al. (2005) and Liu et al. (2008a). In situ zircon U–Pb single-spot dating and trace element analyses, zircon U–Pb age and trace element scanning (mapping), and quartz Ti analysis were conducted using laser ablation inductively coupled plasma mass spectrometry (LA-ICP-MS) at the Mineral Laser Microprobe Analysis Laboratory (Milma Lab), China University of Geosciences (Beijing) (CUGB), described in Zhang et al. (2019) and Jackson. (2008). Zircon grains were analyzed for oxygen isotope ratios ( $\delta^{18}\text{O}$ ) at the secondary ion mass spectrometry (SIMS) Laboratory of Guangzhou Institute of Geochemistry, Chinese Academy of Sciences, and the methodology is detailed in Yang et al. (2018). Zircon Hf isotopic analysis was undertaken at Milma Lab of CUGB, performed by laser ablation multi-collector inductively coupled plasma mass spectrometry (LA-MC-ICP-MS). Detailed descriptions of analytical methods are presented in Supplemental Appendix. 1.

## Results

### Whole-rock geochemical data

Whole-rock geochemical data for 14 samples are given in [Table 1](#). Major element data are normalized on an anhydrous basis after deducting the loss on ignition (LOI = 0.78–2.01 wt%). Like the Nuocang rhyolite and granite porphyry reported by [Jiang et al. \(2018\)](#), located ~25 km southeast of this study ([Fig. 1b](#)), the Nuocang HSR samples are characterized by high SiO<sub>2</sub> content (74.5–79.3 wt%) and low contents of TiO<sub>2</sub> (0.09–0.19 wt%), MgO (0.05–0.19 wt%), and P<sub>2</sub>O<sub>5</sub> (0.03–0.06 wt%) ([Fig. 2](#)). These samples have Al<sub>2</sub>O<sub>3</sub> contents of 11.5–13.4 wt%, and are mostly peraluminous with A/CNK ratios of 1.07–1.35. They have total alkali contents (K<sub>2</sub>O + Na<sub>2</sub>O = 7.12–8.12 wt%) with high K<sub>2</sub>O/Na<sub>2</sub>O ratios of 1.09–3.39, which likely reflect alteration. They are enriched in light rare earth elements (LREE) ([La/Yb]<sub>N</sub> = 11.8–29.8, where N refers to normalization to chondrite values of [Sun and McDonough, 1989](#)) and depleted in heavy rare earth elements (HREE) ([Fig. 3](#)). The Eu anomalies (Eu/Eu\*) are between 0.22 and 0.62.

### Zircon U–Pb ages

Five rhyolite samples 13MD02-1, 13MD03-1, 13MD04-1, 13MD06-2, and 13MD07-1 were chosen for in situ single-spot zircon U–Pb dating by LA-ICP-MS. Sample 13MD07-1 was selected for LA-ICP-MS mapping. The results are listed in Supplemental [Table S1](#) and the concordia plots are shown in [Fig. 4](#).

The zircons in the Nuocang HSRs are mostly euhedral to subhedral prismatic crystals, ~50–150 μm long, with an aspect ratio of 1:1 to 3:1. Unlike the monotonous oscillatory zoning of zircon in the Nuocang granite porphyry reported by [Jiang et al.](#)



(2018), zircons from the Nuocang HSRs show particular internal textural characteristics revealed by cathodoluminescence (CL) images (Fig. 5). Zircons could be classified into two types. The first one has distinct dark-CL cores and light-CL rims of varying thickness, with some cores exhibiting resorption, being truncated by rims. Zircons of this type accounts for more than a third of the total grains in each sample. The second type of zircon has light-CL grain throughout, with no dark-CL core. The light-CL domains in both types of zircons normally display oscillatory growth zoning, and the microscope and CL images of the grains show no hydrothermal features (Hoskin, 2005; Schaltegger, 2007). In addition, the Th/U ratios of all the zircon analyses are greater than 0.1 (0.41–0.83), which is within the range for magmatic zircons (Hoskin and Schaltegger, 2003).

The three kinds of domains, dark-CL cores, light-CL rims, and light-CL grains, were analyzed under the same analytical conditions. The dating results are similar for all three within analytical uncertainty, with no significant discrepancies (Fig. 4f). The zircon  $^{206}\text{Pb}/^{238}\text{U}$  ages of dark-CL cores in all five samples range between 76.2 and 71.5 Ma, with a weighted mean age of  $74.1 \pm 1.6$  Ma ( $n = 39$ , MSWD = 2.8). The light-CL rims and light-CL grains yield  $^{206}\text{Pb}/^{238}\text{U}$  ages range from 78.0 to 72.1 Ma, and 78.0 to 71.5 Ma, respectively, with weighted mean ages of  $74.8 \pm 2.8$  Ma ( $n = 16$ , MSWD = 3.8), and  $74.0 \pm 2.3$  Ma ( $n = 58$ , MSWD = 2.2). Similarly, U–Pb age mapping results demonstrate relatively uniform  $^{206}\text{Pb}/^{238}\text{U}$  ages for all three domains (Fig. 6), considering the analytical uncertainty of 1–5.5 % (Jackson, 2008). These ages are slightly older than the 73.3–72.4 Ma ages for the Nuocang rhyolite and granite porphyry reported by Jiang et al. (2018).

## Zircon trace element composition

In order to avoid the influence of mineral or melt inclusions on the zircon trace element analyses, only spots with smooth signal in the data processing and with <1 chondrite-normalized values for La were selected. The trace element data for 54 spots were obtained, including 30 dark-CL cores, 13 light-CL rims, and 11 light-CL grains and listed in [Table 2](#).

As shown in the chondrite-normalized REE plots ([Fig. 7a](#)), all analyses exhibit typical patterns of magmatic zircons ([Hoskin and Schaltegger, 2003](#); [Corfu et al., 2003](#)). For example, they are LREE-depleted and highly HREE-enriched, and have significant positive Ce and negative Eu anomalies. The light-CL domains, whether rims or whole grains, are significantly different from dark-CL cores ([Fig. 7](#)). The chemical maps in [Fig. 6](#) show the differences in the U, Th, Hf, Y, Ce, and HREE contents between the three zircon domains. The dark-CL cores have U and Th contents of 1117–3799 ppm and 685–2549 ppm, respectively. These are considerably higher than those of the light-CL rims (272–497 ppm and 146–318 ppm, respectively) and light-CL grains (73.0–375 ppm and 47.9–273 ppm, respectively). The Y (2607–7117 ppm) and Hf (12331–15842 ppm) contents and Nb/Ta (3.30–4.82) of the dark-CL cores are higher than those of the light-CL domains (964–1818 ppm, 10746–12192 ppm and 2.58–3.08 for rims, respectively; and 464–1476 ppm, 8571–11736 ppm and 2.26–2.97 for grains, respectively) (see [Table 2](#) and [Fig. 7b, c](#)). However, the Zr/Hf ratios (31.6–40.5) and Eu/Eu\* (0.01–0.06) of the dark-CL cores are lower than light-CL rims (41.0–46.5, 0.05–0.11) and light-CL grains (42.6–58.3, 0.07–0.25) (see [Table 2](#) and [Fig. 7d](#)). The Th/U ratios of

these three domains are roughly the same (0.41–0.83, 0.51–0.69, and 0.60–0.81, respectively). In summary, the dark-CL cores have higher U, Th, Hf and HREE values, and more negative Eu anomaly compared to light-CL rims and light-CL zircon grains.

### **Zircon Hf–O isotopes**

Supplemental **Table S2** summarizes the in situ Hf–O isotopic data of 50 zircon spots from two rhyolite samples (13MD02-1 and 13MD06-2), including 26 dark-CL cores, 6 light-CL rims, and 18 light-CL grains. All analyses yield negative  $\varepsilon_{\text{Hf}}(t)$ , of –8.74 to –5.94 (13MD02-1,  $n = 25$ ), and –9.09 to –5.39 (13MD06-2,  $n = 25$ ). They record a narrower range than the Nuocang granite porphyry ( $\varepsilon_{\text{Hf}}(t) = -22.0$  to –6.00) reported by [Jiang et al. \(2018\)](#). There are no significant differences in zircon  $\varepsilon_{\text{Hf}}(t)$  values between dark-CL cores and light-CL rims and grains (**Fig. 8a**). For example, dark-CL cores yield values between –9.09 and –5.39 ( $n = 26$ ) and crustal model ages ( $T_{\text{DM}}^{\text{C}}$ ) of 1.69–1.46 Ga, compared with light-CL rim values between –8.13 and –5.86 ( $n = 6$ ) with  $T_{\text{DM}}^{\text{C}}$  of 1.63–1.49 Ga, and light-CL grains values between –9.05 and –5.94 ( $n = 18$ ) with  $T_{\text{DM}}^{\text{C}} = 1.69$ –1.49 Ga.

Subtle systematic disparities in the O isotope are observed between the different domains. Compared to those of light-CL domains, the  $\delta^{18}\text{O}$  values of the dark-CL cores are generally lower with smaller variation range (**Fig. 8b**). The  $\delta^{18}\text{O}$  values of dark-CL cores are in the range of 7.77–8.31 ‰, with a mean value of  $8.10 \pm 0.06$  ‰ ( $n = 26$ ). The light-CL rims and grains have  $\delta^{18}\text{O}$  values of 8.06–8.93 ‰ ( $n = 6$ ) and 7.82–9.01 ‰ ( $n = 18$ ), with mean values of  $8.51 \pm 0.27$  ‰ and  $8.51 \pm 0.08$  ‰, respectively. While the dark-CL cores and light-CL domains have different values, in each group there is no

systematic correlation between  $\delta^{18}\text{O}$  values and trace elements (e.g., U, Nb, Lu, Yb) (see Fig. 8b and Table S2).

## Quartz Ti content

This study analyzed contents of trace element in quartz phenocrysts from four samples with particular focus on Ti (samples 13MD02-4, 13MD05-1, 13MD07-1, and 13MD06-2, the latter was also analyzed for Hf–O isotopes in zircons). The results are shown in Fig. 9 and listed in Table 3. Analytical uncertainty is normally less than 15 %. The phenocrysts are subhedral to euhedral and show similar textures in CL images with dark cores and light rims, similar to those reported by Wiebe et al. (2007) and Wark et al. (2007). Two of nine crystals (grains 13MD02-4-2 and 13MD06-2-1 in Table 3) have uniform interior while the others have dark-CL core and light-CL rim. Some of these cores show evidence for resorption (see Supplemental Appendix. 1) and generally have lower Ti contents than the rims. For example, grain 13MD05-1-1 shows that contents of Ti in light-CL rims (37.5–111 ppm) are normally 1-2 times higher than those in dark-CL cores (19.9–55.4 ppm). Grains with uniform CL have more limited spreads of Ti values (e.g., 33.4–55.4 ppm in 13MD06-2-1).

## Discussion

### Reverse zoning zircon: indicator of multi-stage magmatic processes

Although the Nuocang HSRs show high  $\text{SiO}_2$  contents (74.5–79.3 wt%), their high Sr (33.4–88.9 ppm), Ba (252–1461 ppm), Eu/Eu\* (0.22–0.62), Nb/Ta (11.7–15.7), Zr/Hf

(29.0–38.7), and low Rb (97.4–159 ppm), Rb/Sr (1.60–3.73) relative to typical highly-fractionated granites (Gao et al., 2017; Wu et al., 2017) and most HSRs suggest that these rocks are not simply the products of high-degree fractional crystallization. However, the alteration which the Nuocang HSRs experienced makes it difficult to constrain the magmatic evolution using whole-rock geochemistry only. By contrast, zircon and quartz have the potential to preserve some of the record of the long-term evolution of silicic magma system due to their refractory nature and resistance to weathering.

The contents of trace elements of zircon correlate well with the intensity of the CL image (Kempe et al., 2000). This is demonstrated by the mapping results of zircons in this study (Fig. 6). The dark-CL cores have higher U, Th, Hf, Y, and HREE contents and deeper negative Eu anomalies than the light-CL rims (Fig. 7a–d). These differences suggest that the two domains have different parental melt origins. The dark-CL cores with higher U and Th contents, probably crystallized from U- and Th-rich magmas reflecting a high degree of fractional crystallization (Miller and Wooden 2004; Wang et al., 2017; Troch et al., 2018). This is also supported by the more negative Eu anomalies of dark-CL cores (Fig. 7d), which indicate crystallization from a magma that experienced greater fractional crystallization of feldspar. In addition, as the magma differentiated, the Zr/Hf ratios of the melt and consequently of zircons decreased (Claiborne et al. 2006; Samperton et al., 2015; Deering et al., 2016). The decreasing Sm/Yb ratios (Fig. 7e) could be related to the fractionation of MREE-rich accessory minerals such as apatite (Deering et al., 2016). Hence, the dark-CL cores were likely formed in a highly evolved magma, while the light-CL rims crystallized from a less evolved one. Since a detailed

characterization of the accessory phases has not been carried out in this study, it remains possible that the late crystallization of these minerals could modify the melt and impact on zircon chemistry, particularly their REE. However, this cannot explain changes to the Eu/Eu\* values. Besides, the abrupt core-rim changes, rather than gradual variation in content of trace elements, combined with resorption, suggest crystallization of accessory minerals is not the dominant factor to modifying melt and zircon composition. Furthermore, the zoning of our dark core/light rim zircons is opposite to the normal growth pattern resulting from magma cooling. They are thus called reverse zoning zircons (Claiborne et al., 2010b; Reid et al., 2011; Matthews et al., 2015) and reflect multi-stage (at least two stages) magmatic processes. The light-CL section of these composite reverse zoning zircons is similar to our second type of zircons, those entirely comprised of light-CL, in terms of their trace element characteristics (Fig. 7).

Given the estimated analytical uncertainty on SIMS determination of <0.3 ‰ (Yang et al., 2018), the  $\delta^{18}\text{O}$  values of the dark-CL zircon cores (averaging  $8.10 \pm 0.06$  ‰,  $2\sigma$ ,  $n = 26$ ) are collectively lower than those of the light-CL domains (averaging  $8.51 \pm 0.08$  ‰,  $2\sigma$ ,  $n = 24$ ) (Fig. 8b). This difference may indicate the effect of radiation damage of zircon crystal structure, as the dark-CL cores crystallized from U-rich silicic melt, generally show lower  $\delta^{18}\text{O}$  values (Wang et al., 2014). In conclusion, similar U–Pb ages and Hf–O isotopic data indicate that the cores of reverse zoning zircons are most likely not xenocrysts or inherited zircons, but are autocrysts and/or antecrysts (Miller et al., 2007).

### Reheating of magma reservoir revealed by zircon and quartz

Several dark-CL cores show embayment resorption features (Fig. 5) and are truncated by light-CL rims. Variations in the composition or temperature of the magma can change its zircon saturation status (Harrison and Watson, 1983; Boehnke et al., 2013), resulting in their dissolution and reprecipitation (Robinson and Miller, 1999). We argue that after the first-formed zircons (dark-CL cores) were partly dissolved by reheating of the magma, there was renewed zircon crystallization to form the light-CL rims and new grains when the magma cooled again. Given the compositional differences between dark-CL cores and the light-CL zircons, we infer that the new magma was likely hotter than the earlier magma from which the dark-CL cores crystallized. This inference is also supported by the following lines of evidence.

The results of Ti-in-zircon thermometry (Ferry and Watson, 2007) indicate that both the cores and rims of reverse zoning zircon grains have similar crystallization temperature ( $T_{\text{TiZ}}$ ) centered around  $680 \pm 30$  °C, whereas the light-CL grains have a much wider spread, with several grains showing higher temperatures from 740°C to 800 °C (Fig. 7f). We assumed  $\alpha_{\text{SiO}_2} = 1$  and  $\alpha_{\text{TiO}_2} = 0.6$  for the  $T_{\text{TiZ}}$  calculations, according to Watson et al. (2006), considering that quartz is present in Nuocang HSRs and that Ti minerals, such as ilmenite or titanite, are absent. In addition, light-CL grains with the highest  $T_{\text{TiZ}}$  also show the lowest degree of evolution according to their trace element characteristics (Fig. 7b–f). For example, they have the lowest U, Th contents, but the highest Zr/Hf, Sm/Yb ratios and Eu/Eu\* values. Although it is difficult to determine the true  $\alpha_{\text{TiO}_2}$  values, the  $T_{\text{TiZ}}$  trend of the three zircon domains is consistent with the coherent trends defined by trace elements. Thus, the range of temperatures recorded by zircons are interpreted to

reflect the cooling of a high-temperature magma forming light-CL grains as it mixed with a low-temperature, evolved magma containing the dark-CL zircons. Mixing and equilibration between the two led to assimilation of the dark-CL zircons and new growth of light-CL zircon domains.

The quartz CL images and Ti-in-quartz geothermometer further support the conclusions above (e.g., [Wark et al., 2007](#)). Previous studies suggested that the CL brightness of quartz crystals in magmatic rocks is positively correlated with Ti contents (e.g., [Wark and Spear, 2005](#); [Wiebe et al., 2007](#); [Leeman et al., 2012](#)), that increases with the temperature of the magma from which quartz crystallized ([Wark and Watson, 2006](#)). The Ti-in-quartz geothermometer results ([Table 3](#)) demonstrate that similar to the Ti-in-zircon temperatures ( $T_{\text{TiZ}}$ ) for the light-CL grains ([Fig. 7f](#)), the crystallization temperatures (T) of quartz with reverse zoning generally increase from the dark-CL cores to light-CL rims ([Fig. 9d, e](#)). Meanwhile, relatively small variations are noted within quartz crystals with uniform interiors ([Fig. 9f](#)). Although the pressure and Ti activity (e.g., [Thomas et al., 2010](#); [Huang and Audétat, 2012](#)) could also influence the Ti content in zircon and quartz, it is more likely that the reverse zoning combined with resorption features in both minerals in the Nuocang HSRs resulted from changes in the magma temperature during crystallization ([Wark et al., 2007](#); [Shane et al., 2008](#); [Smith et al., 2010](#)). Therefore, both minerals suggest that there was thermal rejuvenation in the Nuocang HSRs magma chamber preceding eruption, which triggered dissolution and reprecipitation of the grains.



## Source of new, hotter and less evolved magma

The  $T_{\text{TiZ}}$  around 680 °C of the dark-CL zircon cores suggests that they crystallized at temperatures close to the eutectic point of granitic magmas. This cold magma was highly evolved, as indicated by zircon composition, possibly a crystal-rich mush. This contrasts with the higher T and less evolved magmas that originated the light-CL zircon domains, and the hotter overgrowth in quartz grains. These findings suggest that a new hotter and less evolved magma intruded, reheated and mix with this evolved mush or crystal rich magma. As it cooled down towards the equilibrium temperature of 680 °C, it gave rise to the reverse zoning zircons and the zoned quartz grains. This initially hotter magma could have been derived either from a new external magma influx or from the re-melting and remobilization of cumulates at depth (Wright et al., 2011; Pamukcu et al., 2013; Wolff et al., 2015; Foley et al., 2020). The dissolution and subsequent new growth of quartz at higher temperatures require increased solidus temperature, which could be achieved in a magma with lower H<sub>2</sub>O activity, caused for example by increased CO<sub>2</sub> (Wark et al., 2007).

The light- and dark-CL domains of the zircons display similar  $\epsilon_{\text{Hf}}(t)$  (Fig. 8a), indicating a common source. Coeval basaltic andesitic tuffs exposed in ~25 km southeast of the Nuocang village (Jiang et al., 2018) (Fig. 1b) could be the heat source. However, it is unlikely that such basaltic andesitic magmatism contributed much mass to the HSRs melts from which the light-CL zircon and quartz grew, because of their uniformity of Hf–O isotopic compositions, which are far from primitive values (McDowell et al., 2016; Foley et al., 2020).

## **Magmatic processes responsible for the formation of Nuocang high-silica rhyolites**

The combined evidence from zircon and quartz suggests that the Nuocang HSRs underwent three evolutionary stages (Fig. 10):

### **Stage 1: Highly evolved magma or crystal-rich mush (Fig. 10a)**

Dark-CL zircons crystallized from a highly evolved magma close to the solidus (i.e., crystal-rich magma or a mush). This is inferred from the trace element features and of the low magmatic temperatures derived from Ti-in-zircon thermometry. The fact that no zircon with light-CL core overgrown by dark-CL rim were found, suggest that the dark-CL zircons started to grow from this evolved magma, indicating that the evolved melt was fractionated and extracted before crystallizing dark-CL zircons.

### **Stage 2: Magma recharge and mixing (Fig. 10b)**

Influx of hotter, less evolved magma into the highly evolved magma chamber and mixing between the two, caused resorption of dark-CL zircons and early formed quartz. The absence of single dark-CL zircons is notable, indicating that reheating of the magma reservoir was sufficient to expose most of the zircon grains. The inflowing less evolved magma would have brought in its own light-CL, high temperature zircons and crystallized quartz rims as it cooled due to mixing with the resident magma/mush, but while still relatively hot. Ti-in-zircon thermometer of the least evolved light-CL grains (Fig. 7f) indicates that the incoming magma was up to 100 °C hotter than the temperature prevalent during dark-CL zircon crystallization.

### **Stage 3: Equilibrium of hybrid magma (Fig. 10c)**

Finally, the two magmas hybridized and cooled back to the equilibrium temperature of 680 °C, leading to further crystallization of light-CL zircons and rims under the same

394  $T_{\text{TiZ}}$  conditions as the original dark-CL zircons, but with a less evolved signature.

395

## 396 **Implications**

397 The two types of zircon recognized in the Nuocang HSRs show similar U–Pb ages  
398 (~74 Ma) and Hf isotopes ( $\epsilon_{\text{Hf}}(t) = -9.09$  to  $-5.39$ ), but have different contents of U, Th,  
399 Hf, Y, HREE and negative Eu anomalies. These features suggest that the cores  
400 crystallized from an evolved melt, but the rims crystallized from a less evolved one.  
401 Ti-in-zircon and Ti-in-quartz geothermometers indicate that the magma was reheated  
402 during crystallization. Bringing the two lines of evidence together, it can be concluded  
403 that instead of being formed as a result of simple fractional crystallization or partial  
404 melting, the the Nuocang HSRs formed as a two-step process where a highly fractionated,  
405 crystal-rich magma was reheated and mixed with a less evolved silica-rich magma prior  
406 to eruption.

407 Our work demonstrates that a combined investigation of zircons and quartz, using  
408 CL images, trace element, and isotopic compositions, can be used to identify multi-stage  
409 magmatic processes. This approach is complementary to and more powerful than  
410 whole-rock and mineral chemistry, particularly when applied to altered rocks.

411 Zircons from silicic volcanic rocks showing dark-CL cores and light-CL rims,  
412 similar to the reverse zoning zircons from the Nuocang HSRs, have also been  
413 documented from a range of different tectonic settings. For example, zircons from  
414 rhyolites of the hot spot-related Lava Creek Tuff in Yellowstone, the extension-related  
415 Bishop Tuff in California and the subduction-related Yandangshan volcanic rocks in SE

China (Bindeman et al., 2008; Reid et al., 2011; Chamberlain et al., 2014; Yan et al., 2018). The results add to the growing use of zircon texture (e.g., reverse zoning), chemistry and isotope signatures in unravelling multi-stage magmatic processes (Claiborne et al., 2006, 2010b; Storm et al., 2014; Rubin et al., 2017).

### Acknowledgments

This work was financially co-supported by the MOST of China (2016YFC0600304), the Second Tibetan Plateau Scientific Expedition and Research Program (STEP) (2019QZKK0702), the 111 project (B18048), and the MOST Special Fund from the State Key Laboratory of Geological Processes and Mineral Resources (China University of Geosciences, Beijing). We thank Calvin Miller and an anonymous reviewer for their thoughtful comments. We thank also Xianhua Li and Xiaolei Wang for help with interpretation of zircon O isotopic data, Jincheng Xie for assistance with zircon mapping images, Rui Wang for greatly improving an early version of the manuscript, and Ying Xia for discussions on magma chamber. This is CUGB petrogeochemical contribution no. PGC2015-0052.

### References cited

- Andersen, T. (2002) Correction of common lead in U–Pb analyses that do not report  $^{204}\text{Pb}$ . Chemical Geology, 192, 59–79.
- Audétat, A. (2013) Origin of Ti-rich rims in quartz phenocrysts from the Upper Bandelier

- 437 Tuff and the Tunnel Spring Tuff, southwestern USA. *Chemical Geology*, 306–361,  
438 99–104.
- 439 Bachmann, O., and Bergantz, G.W. (2008) Rhyolites and their source mushes across  
440 tectonic settings. *Journal of Petrology*, 49, 2277–2285.
- 441 Bernet, M., and Bassett, K. (2005) Provenance analysis by single-quartz-grain  
442 SEM-CL/optical microscopy. *Journal of Sedimentary Research*, 75, 492–500.
- 443 Bindeman, I.N., Fu, B., Kita, N.T., and Valley, J.W. (2008) Origin and evolution of  
444 silicic magmatism at Yellowstone based on ion microprobe analysis of isotopically  
445 zoned zircon. *Journal of Petrology*, 49, 163–193.
- 446 Blichert-Toft, J. (2008) The Hf isotopic composition of zircon reference material 91500.  
447 *Chemical Geology*, 253, 252–257.
- 448 Boehnke, P., Watson, E.B., Trail, D., Harrison, T.M., and Schmitt, A.K. (2013) Zircon  
449 saturation re-revisited. *Chemical Geology*, 351, 324–334.
- 450 Bouvier, A., Vervoort, J.D., and Patchett, P.J. (2008) The Lu–Hf and Sm–Nd isotopic  
451 composition of CHUR: Constraints from unequilibrated chondrites and implications  
452 for the bulk composition of terrestrial planets. *Earth and Planetary Science Letters*,  
453 273, 48–57.
- 454 Chamberlain, K.J., Wilson, C.J.N., Wooden, J.L., Charlier, B.L.A., and Ireland, T.R.  
455 (2014) New perspectives on the Bishop Tuff from zircon textures, ages and trace  
456 elements. *Journal of Petrology*, 55, 395–426.
- 457 Claiborne, L.L., Miller, C.F., Walker, B.A., Wooden, J.L., Mazdab, F.K., and Bea, F.  
458 (2006) Tracking magmatic processes through Zr/Hf ratios in rocks and Hf and Ti  
459 zoning in zircons: An example from the Spirit Mountain batholith, Nevada.

- 460 Mineralogical Magazine, 70, 517–543.
- 461 Claiborne, L.L., Miller, C.F., and Wooden, J.L. (2010a) Trace element composition of  
462 igneous zircon: a thermal and compositional record of the accumulation and  
463 evolution of a large silicic batholith, Spirit Mountain, Nevada. Contributions to  
464 Mineralogy and Petrology, 160, 511–531.
- 465 Claiborne, L.L., Miller, C.F., Flanagan, D.M., Clynnne, M.A., and Wooden, J.L. (2010b)  
466 Zircon reveals protracted magma storage and recycling beneath Mount St. Helens.  
467 Geology, 38, 1011–1014.
- 468 Corfu, F., Hanchar, J.M., Hoskin, P.W.O., and Kinny, P. (2003) Atlas of zircon textures.  
469 Reviews in Mineralogy and Geochemistry, 53, 469–500.
- 470 Deering, C.D., Keller, B., Schoene, B., Bachmann, O., Beane, R., and Ovtcharova, M.  
471 (2016) Zircon record of the plutonic-volcanic connection and protracted rhyolite  
472 melt evolution. Geology, 44, 267–270.
- 473 Ferry, J.M., and Watson, E.B. (2007) New thermodynamic models and revised  
474 calibrations for the Ti-in-zircon and Zr-in-rutile thermometers. Contributions to  
475 Mineralogy and Petrology, 154, 429–437.
- 476 Foley, M.L., Miller, C.F., and Gualda, G.A.R. (2020) Architecture of a super-sized  
477 magma chamber and remobilization of its basal cumulate (Peach Spring Tuff, USA).  
478 Journal of Petrology, in press. DOI <https://doi.org/10.1093/petrology/egaa020>.
- 479 Gao, L.E., Zeng, L.S., and Asimow, P.D. (2017) Contrasting geochemical signatures of  
480 fluid-absent versus fluid-fluxed melting of muscovite in metasedimentary sources:  
481 The Himalayan leucogranites. Geology, 45, 39–42.
- 482 Gao, P., Zheng, Y.F., and Zhao, Z.F. (2016) Experimental melts from crustal rocks: A

483 lithochemical constraint on granite petrogenesis. *Lithos*, 266–267, 133–157.

484 Griffin, W.L., Pearson, N.J., Belousova, E., Jackson, S.E., van Achterbergh, E., O'Reilly,  
485 S.Y., and Shee, S.R. (2000) The Hf isotope composition of cratonic mantle:  
486 LAM-MC-ICPMS analysis of zircon megacrysts in kimberlites. *Geochimica et*  
487 *Cosmochimica Acta*, 64, 133–147.

488 Griffin, W.L., Wang, X., Jackson, S.E., Pearson, N.J., O'Reilly, S.Y., Xu, X.S., and Zhou,  
489 X.M. (2002) Zircon chemistry and magma mixing, SE China: In-situ analysis of Hf  
490 isotopes, Tonglu and Pingtan igneous complexes. *Lithos*, 61, 237–269.

491 Gualda, G.A.R., and Ghiorso, M.S. (2013) Low-pressure origin of high-silica rhyolites  
492 and granites. *The Journal of Geology*, 121, 537–545.

493 Harrison, T.M., and Watson, E.B. (1983) Kinetics of zircon dissolution and zirconium  
494 diffusion in granitic melts of variable water content. *Contributions to Mineralogy*  
495 *and Petrology*, 84, 66–72.

496 Hoskin, P.W.O., and Schaltegger, U. (2003) The composition of zircon and igneous and  
497 metamorphic petrogenesis. *Reviews in Mineralogy and Geochemistry*, 53, 27–62.

498 Hoskin, P.W.O. (2005) Trace-element composition of hydrothermal zircon and the  
499 alteration of Hadean zircon from the Jack Hills, Australia. *Geochimica et*  
500 *Cosmochimica Acta*, 69, 637–648.

501 Huang, R.F., and Audétat, A. (2012) The titanium-in-quartz (TitaniQ) thermobarometer:  
502 A critical examination and re-calibration. *Geochimica et Cosmochimica Acta*, 84,  
503 75–89.

504 Jackson, S.E., Pearson, N.J., Griffin, W.L., and Belousova, E.A. (2004) The application  
505 of laser ablation-inductively coupled plasma-mass spectrometry to in situ U–Pb

- 506 zircon geochronology. *Chemical Geology*, 211, 47–69.
- 507 Jackson, S. (2008) LAMTRACE Data Reduction Software for LA-ICP-MS. In P.  
508 Sylvester, Ed., *Laser Ablation ICP-MS in The Earth Sciences: Current Practices and*  
509 *Outstanding Issues*, p. 305–307. Mineralogical Association of Canada.
- 510 Ji, W.Q., Wu, F.Y., Chung, S.L., Li, J.X., and Liu, C.Z. (2009) Zircon U–Pb  
511 geochronology and Hf isotopic constraints on the petrogenesis of the Gangdese  
512 batholith, southern Tibet. *Chemical Geology*, 262, 229–245.
- 513 Jiang, J.S., Zheng, Y.Y., Gao, S.B., Zhang, Y.C., Huang, J., Liu, J., Wu, S., Xu, J., and  
514 Huang, L.L. (2018) The newly-discovered Late Cretaceous igneous rocks in the  
515 Nuocang district: Products of ancient crust melting triggered by Neo-Tethyan slab  
516 rollback in the western Gangdese. *Lithos*, 308–309, 294–315.
- 517 Keller, C.B., Schoene, B., Barboni, M., Samperton, K.M., and Husson, J.M. (2015)  
518 Volcanic-plutonic parity and the differentiation of the continental crust. *Nature*, 523,  
519 301–307.
- 520 Kemp, A.I.S., Hawkesworth, C.J., Foster, G.L., Paterson, B.A., Woodhead, J.D., Hergt,  
521 J.M., Gray, C.M., and Whitehouse, M.J. (2007) Magmatic and crustal differentiation  
522 history of granitic rocks from Hf–O isotopes in zircon. *Science*, 315, 980–983.
- 523 Kempe, U., Gruner, T., Nasdala, L., and Wolf, D. (2000) Relevance of  
524 cathodoluminescence for the interpretation of U–Pb zircon ages, with an example of  
525 an application to a study of zircons from the Saxonian granulite complex, Germany.  
526 In M. Pagel, V. Barbin, P. Blanc, D. and Ohnenstetter, Eds., *Cathodoluminescence*  
527 *in Geosciences*, p. 415–455. Springer, Berlin, Heidelberg.
- 528 Lee, C-T.A., and Morton, D.M. (2015) High silica granites: Terminal porosity and crystal



529 settling in shallow magma chambers. *Earth and Planetary Science Letters*, 409,  
530 23–31.

531 Leeman, W.P., MacRae, C.M., Wilson, N.C., Torpy, A., Lee, C-T.A., Student, J.J.,  
532 Thomas, J.B. and Vicenzi, E.P. (2012) A study of cathodoluminescence and trace  
533 element compositional zoning in natural quartz from volcanic rocks: Mapping  
534 titanium content in quartz. *Microscopy and Microanalysis*, 18, 1322–1341.

535 Liu, Y.S., Zong, K.Q., Kelemen, P.B., and Gao, S. (2008a) Geochemistry and magmatic  
536 history of eclogites and ultramafic rocks from the Chinese continental scientific drill  
537 hole: Subduction and ultrahigh-pressure metamorphism of lower crustal cumulates.  
538 *Chemical Geology*, 247, 133–153.

539 Liu, Y.S., Hu, Z.C., Gao, S., Günther, D., Xu, J., Gao, C.G., and Chen, H.H. (2008b) In  
540 situ analysis of major and trace elements of anhydrous minerals by LA-ICP-MS  
541 without applying an internal standard. *Chemical Geology*, 257, 34–43.

542 Liu, Y.S., Hu, Z.C., Zong, K.Q., Gao, C.G., Gao, S., Xu, J., and Chen, H.H. (2010)  
543 Reappraisal and refinement of zircon U–Pb isotope and trace element analyses  
544 by LA-ICP-MS. *Chinese Science Bulletin*, 55, 1535–1546.

545 Ludwig, K. R. (2012) User’s Manual for Isoplot 3.75, a Geochronological Toolkit for  
546 Microsoft Excel. Berkeley Geochronology Center Special Publication, Berkeley,  
547 California, no. 5 (75 pp.).

548 Matthews, N.E., Vazquez, J.A., and Calvert, A.T. (2015) Age of the Lava Creek  
549 supereruption and magma chamber assembly at Yellowstone based on  $^{40}\text{Ar}/^{39}\text{Ar}$  and  
550 U–Pb dating of sanidine and zircon crystals. *Geochemistry, Geophysics,*  
551 *Geosystems*, 16, 2508–2528.

- 552 McDowell, S.M., Overton, S., Fisher, C.M., Frazier, W.O., Miller, C.F., Miller, J.S., and  
553 Economos, R.C. (2016). Hafnium, oxygen, neodymium, strontium, and lead isotopic  
554 constraints on magmatic evolution of the supereruptive southern Black Mountains  
555 volcanic center, Arizona, U.S.A.: A combined LASS zircon-whole-rock study.  
556 American Mineralogist, 101, 311–327.
- 557 Miller, J.S., and Wooden, J.L. (2004) Residence, resorption and recycling of zircons in  
558 Devils Kitchen rhyolite, Coso Volcanic field, California. Journal of Petrology, 45,  
559 2155–2170.
- 560 Miller, J.S., Matzel, J.E.P., Miller, C.F., Burgess, S.D., and Miller, R.B. (2007) Zircon  
561 growth and recycling during the assembly of large, composite arc plutons. Journal of  
562 Volcanology and Geothermal Research, 167, 282–299.
- 563 Moyen, J.F., Laurent, O., Chelle-Michou, C., Couzinié, S., Vanderhaeghe, O., Zeh, A.,  
564 Villaros, A., and Gardien, V. (2017) Collision vs. subduction-related magmatism:  
565 Two contrasting ways of granite formation and implications for crustal growth.  
566 Lithos, 277, 154–177.
- 567 Nandedkar, R.H., Ulmer, P., and Müntener, O. (2014) Fractional crystallization of  
568 primitive, hydrous arc magmas: an experimental study at 0.7 GPa. Contributions to  
569 Mineralogy and Petrology, 167, 1015.
- 570 Pamukcu, A.S., Carley, T.L., Gualda, G.A.R., Miller, C.F., and Ferguson, C.A. (2013)  
571 The evolution of the Peach Spring giant magma body: evidence from accessory  
572 mineral textures and compositions, bulk pumice and glass geochemistry, and  
573 Rhyolite-MELTS modeling. Journal of Petrology, 54, 1109–1148.
- 574 Pan, G.T., Ding, J., Yao, D.S., and Wang, L.Q. (2004) Guidebook of 1:1500000

575 geological map of the Qinghai-Xizang (Tibet) plateau and adjacent areas.  
576 Cartographic Publishing House, Chengdu, China.

577 Paton, C., Hellstrom, J., Paul, B., Woodhead, J., and Hergt, J. (2011) Iolite: Freeware for  
578 the visualisation and processing of mass spectrometric data. *Journal of Analytical*  
579 *Atomic Spectrometry*, 26, 2508–2518.

580 Reid, M.R., Vazquez, J.A., and Schmitt, A.K. (2011) Zircon-scale insights into the  
581 history of a Supervolcano, Bishop Tuff, Long Valley, California, with implications  
582 for the Ti-in-zircon geothermometer. *Contributions to Mineralogy and Petrology*,  
583 161, 293–311.

584 Robinson, D.M., and Miller, C.F. (1999) Record of magma chamber processes preserved  
585 in accessory mineral assemblages. *American Mineralogist*, 84, 1346–1353.

586 Rubin, A.E., Cooper, K.M., Till, C.B., Kent, A.J.R., Costa, F., Bose, M., Gravley, D.,  
587 Deering, C., and Cole, J. (2017) Rapid cooling and cold storage in a silicic magma  
588 reservoir recorded in individual crystals. *Science*, 356, 1154–1156.

589 Samperton, K.M., Schoene, B., Cottle, J.M., Keller, C.B., Crowley, J.L., and Schmitz,  
590 M.D. (2015) Magma emplacement, differentiation and cooling in the middle crust:  
591 Integrated zircon geochronological-geochemical constraints from the Bergell  
592 Intrusion, Central Alps. *Chemical Geology*, 417, 322–340.

593 Schaltegger, U. (2007) Hydrothermal zircon. *Elements*, 3, 51–79.

594 Schiano, P., Monzier, M., Eissen, J.P., Martin, H., and Koga, K.T. (2010) Simple mixing  
595 as the major control of the evolution of volcanic suites in the Ecuadorian Andes.  
596 *Contributions to Mineralogy and Petrology*, 160, 297–312.

597 Shane, P., Smith, V.C., and Nairn, I. (2008) Millennial timescale resolution of rhyolite

598 magma recharge at Tarawera volcano: insights from quartz chemistry and melt  
599 inclusions. *Contributions to Mineralogy and Petrology*, 156, 397–411.

600 Simakin, A.G., and Bindeman, I.N. (2012) Remelting in caldera and rift environments  
601 and the genesis of hot, “recycled” rhyolites. *Earth and Planetary Science Letters*,  
602 337–338, 224–235.

603 Sisson, T.W., Ratajeski, K., Hankins, W.B., and Glazner, A.F. (2005) Voluminous  
604 granitic magmas from common basaltic sources. *Contributions to Mineralogy and*  
605 *Petrology*, 148, 635–661.

606 Sláma, J., Košler, J., Condon, D.J., Crowley, J.L., Gerdes, A., Hanchar, J.M. Matthew,  
607 S.A.H, Morris, G.A., Nasdala, L., Norberg, N., Schaltegger, U., Schoene, B, Tubrett,  
608 M.N., and Whitehouse, M.J. (2008) Plešovice zircon — A new natural reference  
609 material for U–Pb and Hf isotopic microanalysis. *Chemical Geology*, 249, 1–35.

610 Smith, V., Shane, P., and Nairn, I. (2010) Insights into silicic melt generation using  
611 plagioclase, quartz and melt inclusions from the caldera-forming Rotoiti eruption,  
612 Taupo volcanic zone, New Zealand. *Contributions to Mineralogy and Petrology*, 160,  
613 951–971.

614 Söderlund, U., Patchett, P.J., Vervoort, J.D., and Isachsen, C.E. (2004) The  $^{176}\text{Lu}$  decay  
615 constant determined by Lu–Hf and U–Pb isotope systematics of Precambrian mafic  
616 intrusions. *Earth and Planetary Science Letters*, 219, 311–324.

617 Storm, S., Schmitt, A.K., Shane, P., and Lindsay, J.M. (2014) Zircon trace element  
618 chemistry at sub-micrometer resolution for Tarawera volcano, New Zealand, and  
619 implications for rhyolite magma evolution. *Contributions to Mineralogy and*  
620 *Petrology*, 167, 1000.

- 621 Streck, M.J. (2002) Partial melting to produce high-silica rhyolites of a young bimodal  
622 suite: compositional constraints among rhyolites, basalts, and metamorphic xenoliths  
623 from the Harney Basin, Oregon. *International Journal of Earth Sciences*, 91,  
624 583–593.
- 625 Sun, S.S., and McDonough, W.F. (1989) Chemical and isotope systematics of oceanic  
626 basalts: implications for mantle composition and processes. *Geological Society*,  
627 London, Special Publications, 42, 313–345.
- 628 Tang, Y.W., Chen, L., Zhao, Z.F., and Zheng, Y.F. (2019) Geochemical evidence for the  
629 production of granitoids through reworking of the juvenile mafic arc crust in the  
630 Gangdese orogen, southern Tibet. *Geological Society of America Bulletin*, in press.  
631 DOI <https://doi.org/10.1130/B35304.1>.
- 632 Thomas, J.B., Watson, E.B., Spear, F.S., Shemella, P.T., Nayak, S.K., and Lanzirotti, A.  
633 (2010) TitaniQ under pressure: the effect of pressure and temperature on the  
634 solubility of Ti in quartz. *Contributions to Mineralogy and Petrology*, 160, 743–759.
- 635 Troch, J., Ellis, B.S., Schmitt, A.K., Bouvier, A-S., and Bachmann, O. (2018) The dark  
636 side of zircon: textural, age, oxygen isotopic and trace element evidence of fluid  
637 saturation in the subvolcanic reservoir of the Island Park-Mount Jackson Rhyolite,  
638 Yellowstone (USA). *Contributions to Mineralogy and Petrology*, 173, 54.
- 639 Wang, D., Wang, X.L., Cai, Y., Chen, X., Zhang, F.R., and Zhang, F.F. (2017)  
640 Heterogeneous conservation of zircon xenocrysts in Late Jurassic granitic intrusions  
641 within the Neoproterozoic Jiuling batholith, south China: a magma chamber growth  
642 model in deep crustal hot zones. *Journal of Petrology*, 58, 1781–1810.
- 643 Wang, X.L., Coble, M.A., Valley, J.W., Shu, X.J., Kitajima, K., Spicuzza, M.J., and Sun,

- 644 T. (2014) Influence of radiation damage on Late Jurassic zircon from southern  
645 China: Evidence from in situ measurements of oxygen isotopes, laser Raman, U–Pb  
646 ages, and trace elements. *Chemical Geology*, 389, 122–136.
- 647 Wark, D.A., and Spear, F.S. (2005) Ti in quartz: Cathodoluminescence and thermometry.  
648 *Geochimica et Cosmochimica Acta*, Supplement, 69, A592.
- 649 Wark, D.A., and Watson, E.B. (2006) TitaniQ: a titanium-in-quartz geothermometer.  
650 *Contributions to Mineralogy and Petrology*, 152, 743–754.
- 651 Wark, D.A., Hildreth, W., Spear, F.S., Cherniak, D.J., and Watson, E.B. (2007)  
652 Pre-eruption recharge of the Bishop magma system. *Geology*, 35, 235–238.
- 653 Watson, E.B., Wark, D.A., and Thomas, J.B. (2006) Crystallization thermometers for  
654 zircon and rutile. *Contributions to Mineralogy and Petrology*, 151, 413.
- 655 Wiebe, R.A., Wark, D.A., and Hawkins, D.P. (2007) Insights from quartz  
656 cathodoluminescence zoning into crystallization of the Vinalhaven granite, coastal  
657 Maine. *Contributions to Mineralogy and Petrology*, 154, 439–453.
- 658 Wolff, J.A., Ellis, B.S., Ramos, F.C., Starkel, W.A., Borroughs, S., Olin, P.H., and  
659 Bachmann, O. (2015) Remelting of cumulates as a process for producing chemical  
660 zoning in silicic tuffs: A comparison of cool, wet and hot, dry rhyolitic magma  
661 systems. *Lithos*, 236–237, 275–286.
- 662 Wright, H.M.N., Folkes C.B., Cas, R.A.F., and Cashman, K.V. (2011) Heterogeneous  
663 pumice populations in the 2.08-Ma Cerro Galán Ignimbrite: implications for magma  
664 recharge and ascent preceding a large-volume silicic eruption. *Bulletin of*  
665 *Volcanology*, 73, 1513–1533.
- 666 Wu, F.Y., Liu, X.C., Ji, W.Q., Wang, J.M., and Yang, L. (2017) Highly fractionated

- 667 granites: Recognition and research. *Science China Earth Sciences*, 47, 745-765.
- 668 Yan, L.L., He, Z.Y., Beier, C., and Klemd, R. (2018) Zircon trace element constrains on  
669 the link between volcanism and plutonism in SE China. *Lithos*, 320–321, 28–34.
- 670 Yang, J.H., Chung, S.L., Wilde, S.A., Wu, F.Y., Chu, M.F., Lo, C.H., and Fan, H.R. (2005)  
671 Petrogenesis of post-orogenic syenites in the Sulu Orogenic Belt, East China:  
672 geochronological, geochemical and Nd–Sr isotopic evidence. *Chemical Geology*,  
673 214, 99–125.
- 674 Yang, J.H., Wu, F.Y., Wilde, S.A., Xie, L.W., Yang, Y.H., and Liu, X.M. (2007) Tracing  
675 magma mixing in granite genesis: in situ U–Pb dating and Hf-isotope analysis of  
676 zircons. *Contributions to Mineralogy and Petrology*, 153, 177–190.
- 677 Yang, Q., Xia, X.P., Zhang, W.F., Zhang, Y.Q., Xiong, B.Q., Xu, Y.G., Wang, Q., and Wei,  
678 G.J. (2018) An evaluation of precision and accuracy of SIMS oxygen isotope  
679 analysis. *Solid Earth Sciences*, 3, 81–86.
- 680 Zhang, L.L., Zhu, D.C., Wang, Q., Zhao, Z.D., Liu, D., and Xie, J.C. (2019) Late  
681 Cretaceous volcanic rocks in the Sangri area, southern Lhasa Terrane, Tibet:  
682 Evidence for oceanic ridge subduction. *Lithos*, 326–327, 144–157.
- 683 Zhang, Z.M., Zhao, G.C., Santosh, M., Wang, J.L., Dong, X., and Shen, K. (2010) Late  
684 Cretaceous charnockite with adakitic affinities from the Gangdese batholith,  
685 southeastern Tibet: Evidence for Neo-Tethyan mid-ocean ridge subduction?  
686 *Gondwana Research*, 17, 615–631.
- 687 Zhang, Z.M., Ding, H.X., Palin, R.M., Dong, X., Tian, Z.L., and Chen, Y.F. (2020) The  
688 lower crust of the Gangdese magmatic arc, southern Tibet, implication for the  
689 growth of continental crust. *Gondwana Research*, 77, 136–146.

690 Zhu, D.C., Zhao, Z.D., Niu, Y.L., Mo, X.X., Chung, S.L., Hou, Z.Q., Wang, L.Q., and  
691 Wu, F.Y. (2011) The Lhasa Terrane: Record of a microcontinent and its histories of  
692 drift and growth. *Earth and Planetary Science Letters*, 301, 241–255.

693 Zhu, D.C., Zhao, Z.D., Niu, Y.L., Dilek, Y., Hou, Z.Q., and Mo, X.X. (2013) The origin  
694 and pre-Cenozoic evolution of the Tibetan Plateau. *Gondwana Research*, 23,  
695 1429–1454.

696



## Figure captions

- Figure 1.** (a)–(b) Simplified tectonic framework of the Tibetan Plateau showing major tectonic subdivisions and further divisions of the Lhasa Terrane (Zhu et al. 2013). Rectangles shows the position of (b) and (c). (c) Geological map of the Nuocang area (modified after the Regional Geological Survey Map 1: 250000 Coqin Sheet, H45C002001, 2003). (d) Field photograph of volcanic rocks in the Nuocang area. (e)–(g) Representative photomicrographs for Nuocang HSR samples. Abbreviations: JSSZ = Jinsha Suture Zone, LSSZ = Longmu Tso-Shuanghu Suture Zone, BNSZ = Bangong-Nujiang Suture Zone, SNMZ = Shiquan River-Nam Tso Mélange Zone, LMF = Luobadui-Milashan Fault Zone, IYZSZ = Indus-Yarlung Zangbo Suture Zone, NL = northern Lhasa subterrane, CL = central Lhasa subterrane, SL = southern Lhasa subterrane, Kfs = K-feldspar, Pl = plagioclase, Q = quartz.
- Figure 2.** Selected Harker diagrams for samples from the Nuocang HSRs, and for basaltic andesite tuff, rhyolites, granite porphyry from the same region, reported by Jiang et al. (2018).
- Figure 3.** Chondrite-normalized REE patterns and primitive-mantle-normalized trace element patterns for the samples from Nuocang HSRs, and for basaltic andesite tuff, rhyolites, and granite porphyry from Jiang et al. (2018). Chondrite and primitive mantle values are from Sun and McDonough (1989).
- Figure 4.** Zircon U–Pb concordia plots of five samples from the Nuocang HSRs. Dashed circles on CL images indicate the analytical spots of LA-ICP-MS U–Pb dating.
- Figure 5.** Representative cathodoluminescence (CL) images of zircons from Nuocang

HSR samples (sample labels are given in upper right of each image). Note two types of zircons: one having dark-CL cores and light-CL rims, the other formed entirely by light-CL zircons, lacking dark cores.

**Figure 6.** Representative CL, LA-ICP-MS  $^{206}\text{Pb}/^{238}\text{U}$  age and trace element mapping images of zircons from sample 13MD07-1.

**Figure 7. (a)** Chondrite-normalized REE patterns of zircons from Nuocang HSRs. Data for normalization are from [Sun and McDonough \(1989\)](#). **(b)–(f)** Selected trace element compositions and Ti-in-zircon temperatures ( $T_{\text{TiZ}}$ ) of zircons from Nuocang HSRs. It was assumed that  $\alpha_{\text{SiO}_2} = 1$  and  $\alpha_{\text{TiO}_2} = 0.6$ , following [Watson et al. \(2006\)](#) considering that quartz is present and Ti minerals such as ilmenite or titanite are absent in the Nuocang HSRs. Zircon domains with the highest  $T_{\text{TiZ}}$  values, surrounded by the pink dashed lines in the figures, also have the highest Eu/Eu\* and Sm/Yb ratios, but the lowest contents of U, Y, Hf.

**Figure 8.** Hf–O isotopic data vs. U contents of zircons from Nuocang HSRs. The pink rectangles are for  $\epsilon_{\text{Hf}}(t)$  and  $\delta^{18}\text{O}$  ranges of zircon dark-CL cores. Analytical uncertainty of zircon  $\delta^{18}\text{O}$  values ( $2\sigma$ ) is normally  $< 0.3\text{‰}$ .

**Figure 9.** Representative CL images of three quartz phenocrysts **(a)–(c)** and the results of Ti-in-quartz geothermometry calculation (T) **(d)–(f)** according to [Wark and Watson \(2006\)](#), assuming  $\alpha_{\text{TiO}_2} = 0.6$ . Solid and dashed circles represent analytical spot diameters of 50 and 75  $\mu\text{m}$ , respectively. More CL images of quartz phenocrysts are represented in Supplemental [Appendix. 1](#).

**Figure 10.** Schematic illustrations showing the three-stage evolution for producing Nuocang HSRs. See detailed description in discussion in the main text.

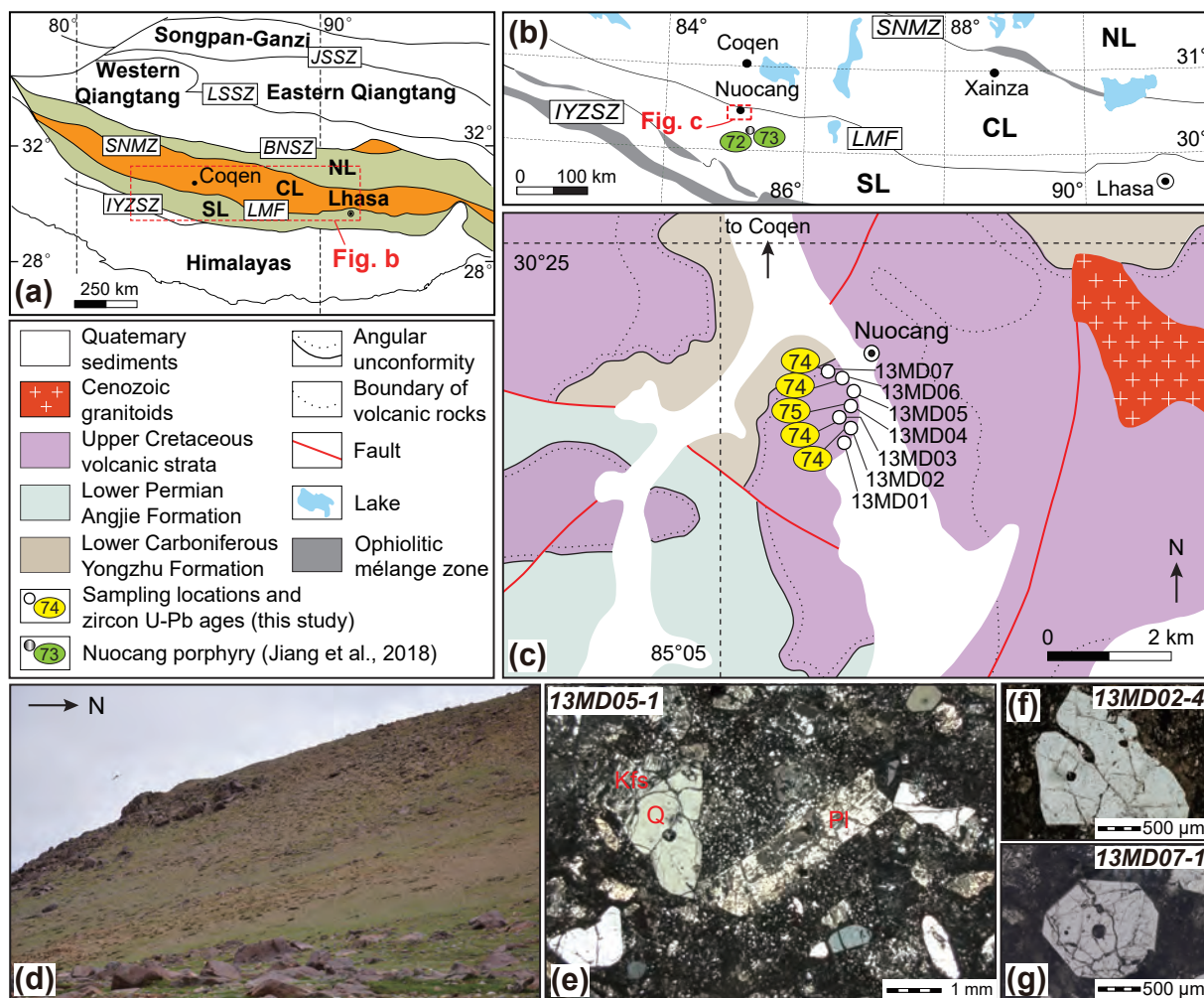
## Table captions

**Table 1.** Whole-rock major and trace element data of the Nuocang HSR samples in the southern Lhasa subterrane.

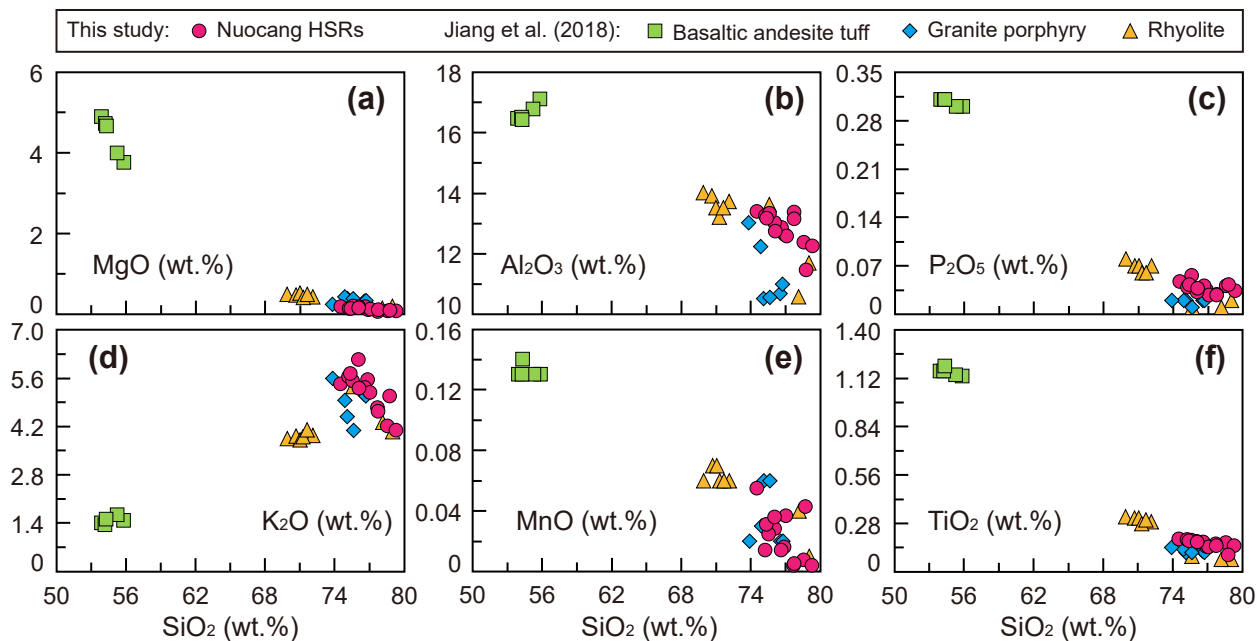
**Table 2.** LA-ICP-MS zircon trace element data of the Nuocang HSR samples.

**Table 3.** LA-ICP-MS quartz Ti content and geothermometer calculation results of the Nuocang HSR samples. Abbreviations: DC = dark-CL core, LR = light-CL rim, M = mantle, which is transition zone between DC and LR, and similar to LR.

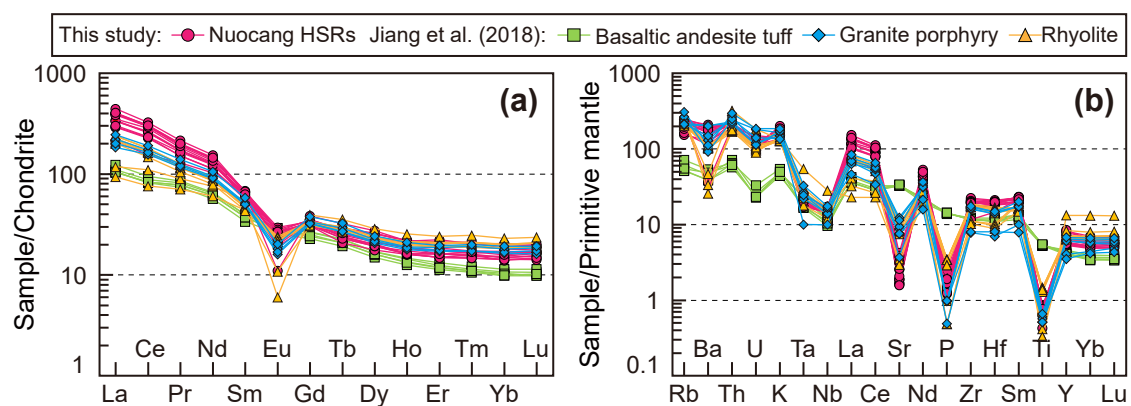
## Chen et al.' s **Figure 1**: W 160 mm – H 132mm



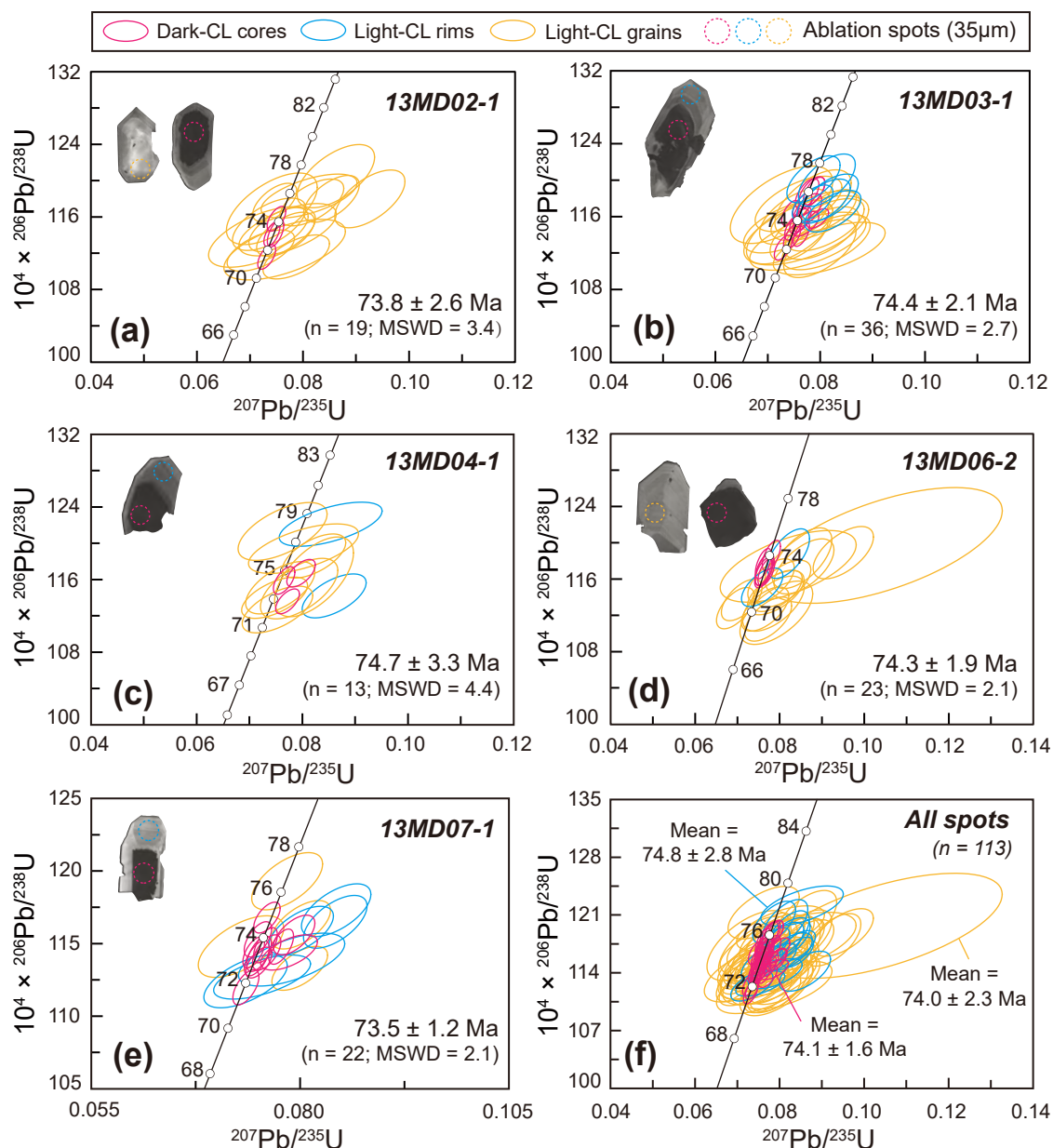
## Chen et al.' s **Figure 2**: W 165 mm – H 84 mm



## Chen et al.' s **Figure 3**: W 148 mm – H 52 mm

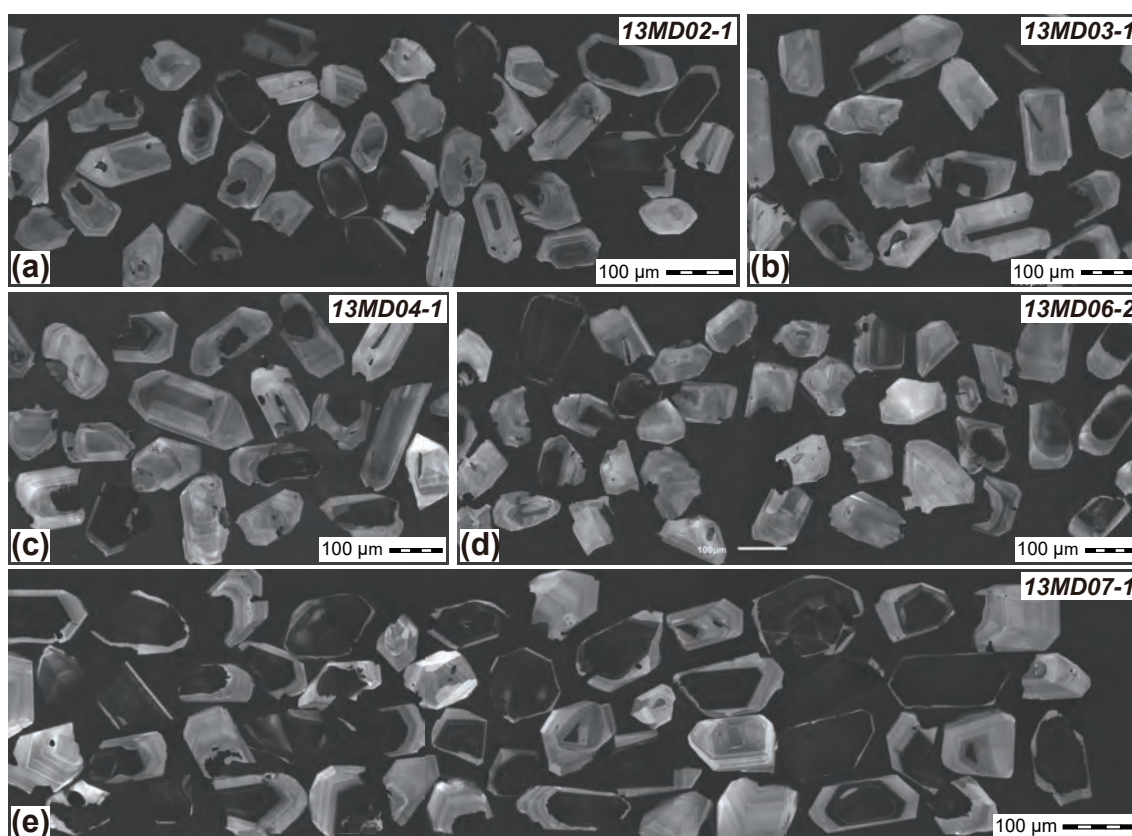


## Chen et al.' s **Figure 4**: W 150 mm – H 163 mm



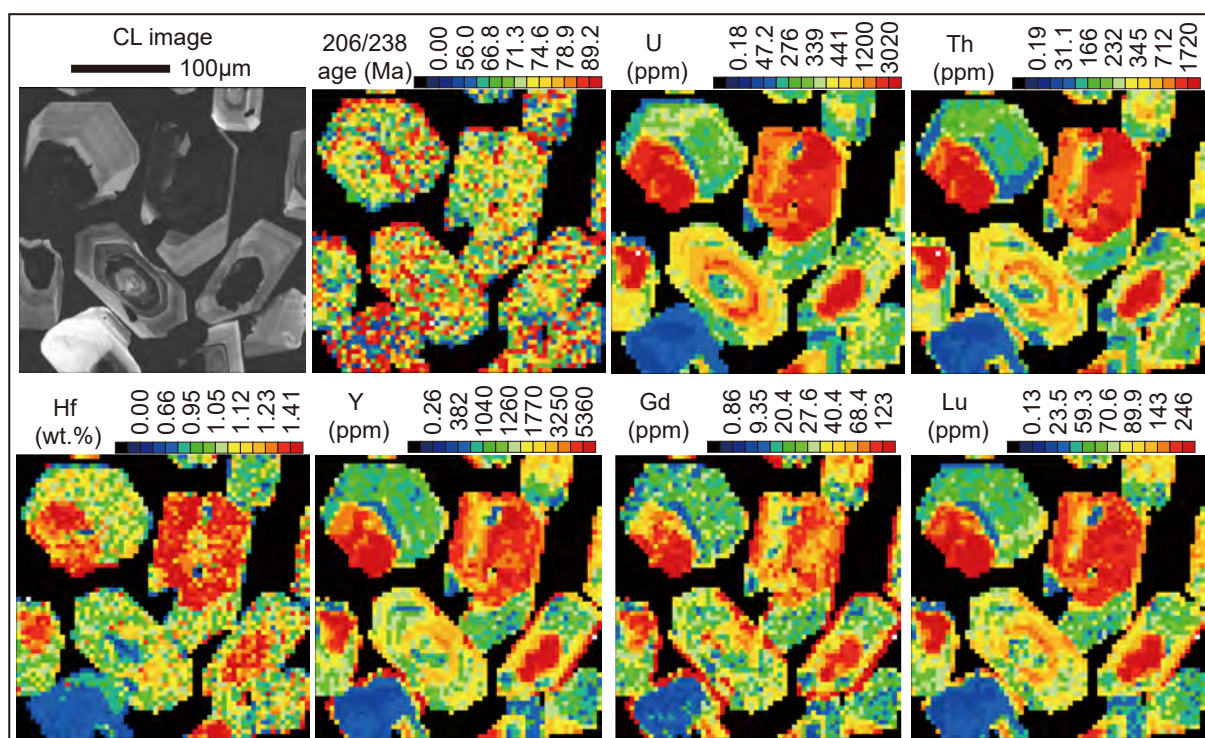


## Chen et al.' s **Figure 5**: W 150 mm - H 110mm

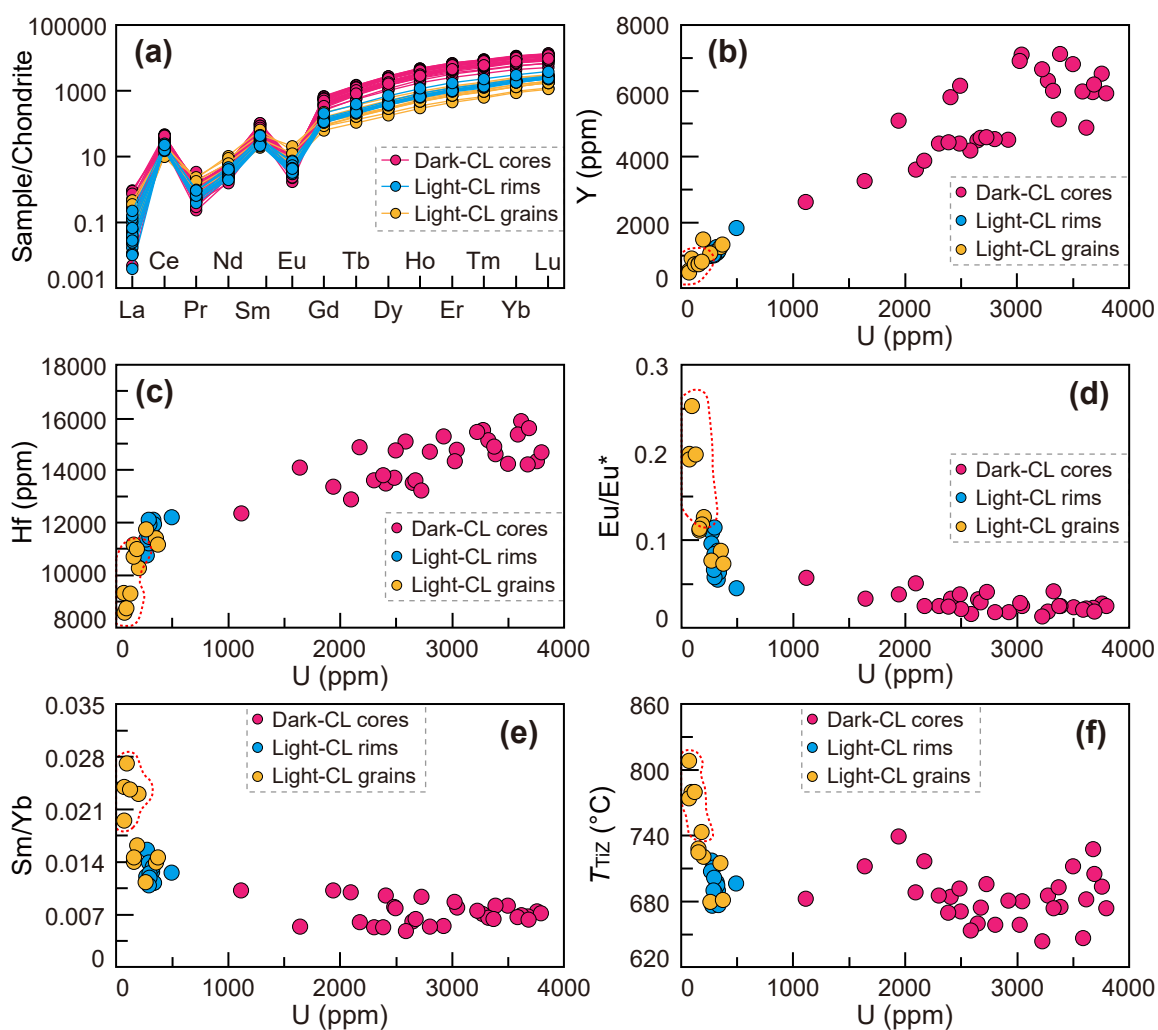




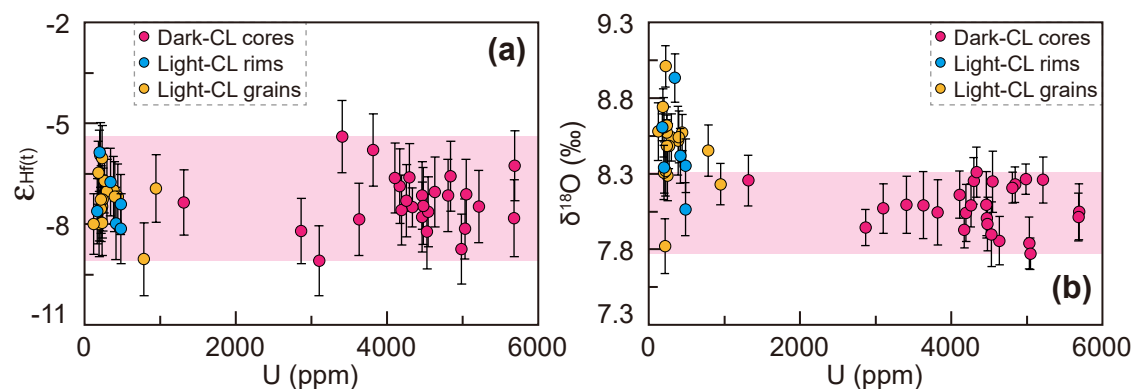
## Chen et al.' s **Figure 6:** W 160 mm - H 97 mm



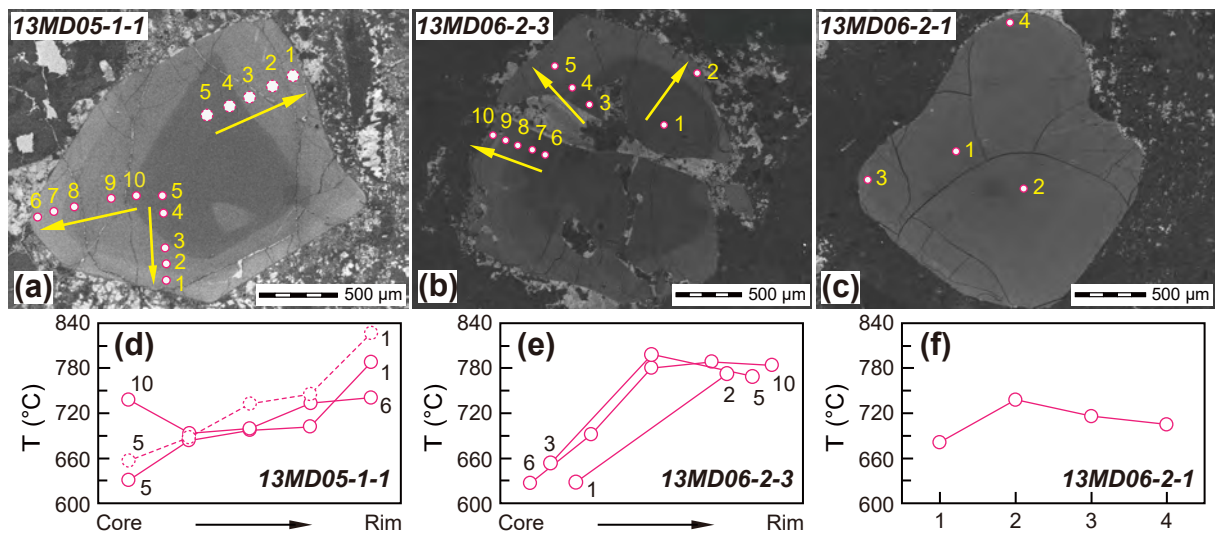
## Chen et al.' s **Figure 7**: W 152 mm – H 135 mm



## Chen et al.' s **Figure 8**: W 150 mm – H 50 mm



## Chen et al.' s **Figure 9**: W 160 mm – H 70 mm



## Chen et al.' s **Figure 10**: W 160 mm – H 52 mm

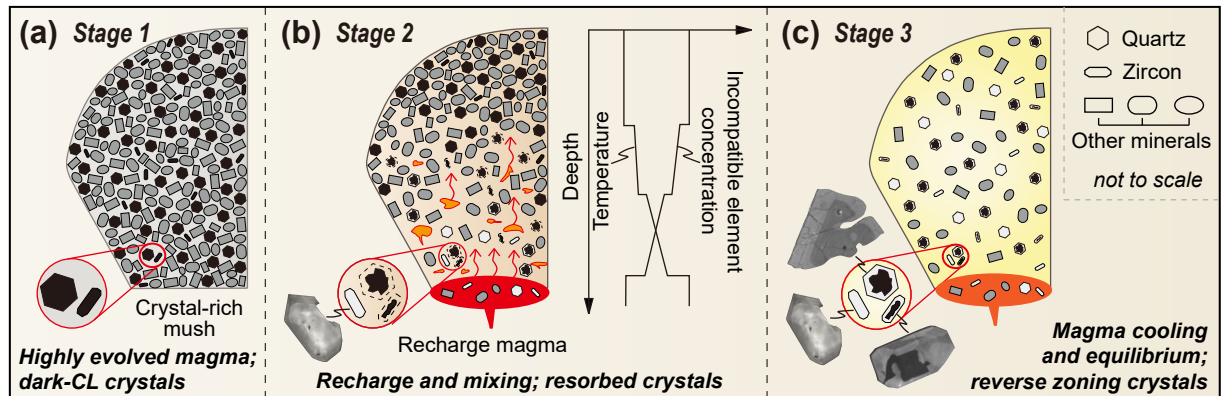


**Table 1. Whole-rock major and trace element data of the Nuocang HSR samples**

Sample no.	13MD01-1	13MD02-1	13MD02-3	13MD02-4	13MD03-1	13MD03-2	13MD03-3
Lithology	Rhyolite	Rhyolite	Rhyolite	Rhyolite	Rhyolite	Rhyolite	Rhyolite
<b>Major element (wt.%)</b>							
<b>SiO<sub>2</sub></b>	76.9	78.6	79.3	77.7	76.6	74.5	77.1
<b>TiO<sub>2</sub></b>	0.15	0.16	0.15	0.16	0.17	0.19	0.14
<b>Al<sub>2</sub>O<sub>3</sub></b>	12.7	12.4	12.3	13.4	12.9	13.4	12.6
<b>TFe<sub>2</sub>O<sub>3</sub></b>	2.02	0.54	0.47	0.39	2.23	2.25	1.54
<b>MnO</b>	0.02	0.01	0.00	0.00	0.01	0.05	0.04
<b>MgO</b>	0.10	0.07	0.07	0.05	0.17	0.17	0.12
<b>CaO</b>	0.22	0.14	0.12	0.13	0.25	1.34	0.90
<b>Na<sub>2</sub>O</b>	2.37	3.86	3.49	3.38	2.27	2.59	2.38
<b>K<sub>2</sub>O</b>	5.56	4.22	4.09	4.74	5.33	5.44	5.19
<b>P<sub>2</sub>O<sub>5</sub></b>	0.03	0.04	0.03	0.03	0.04	0.05	0.03
<b>LOI</b>	1.07	0.78	0.84	1.02	1.17	2.01	1.59
<b>TOTAL</b>	99.9	99.9	99.9	99.8	99.8	99.8	99.8
<b>Trace element (ppm)</b>							
<b>Li</b>	8.87	8.73	8.63	24.4	7.31	8.95	11.2
<b>Be</b>	2.15	1.12	1.38	1.30	2.24	2.57	2.04
<b>Sc</b>	6.24	4.88	4.88	6.21	6.26	7.27	6.27
<b>V</b>	9.89	7.62	6.77	9.35	9.87	10.8	5.20
<b>Cr</b>	0.53	0.93	0.88	1.01	0.70	0.44	0.33
<b>Co</b>	0.39	1.03	0.13	0.12	0.42	0.55	0.54
<b>Ni</b>	1.28	1.72	1.39	1.30	1.35	1.10	1.43
<b>Cu</b>	1.49	1.16	1.15	0.90	1.26	2.13	2.43
<b>Zn</b>	33.0	8.29	9.55	9.52	32.1	36.3	37.0
<b>Ga</b>	16.8	13.7	15.2	16.7	17.7	18.8	17.7
<b>Rb</b>	148	97.4	103	117	142	142	133
<b>Sr</b>	40.3	35.2	33.6	35.7	39.4	88.9	39.5
<b>Y</b>	29.4	24.1	26.8	35.8	24.8	25.5	37.1
<b>Zr</b>	183	213	193	226	217	240	189
<b>Nb</b>	11.1	10.6	10.6	12.4	11.2	12.2	11.9
<b>Cs</b>	4.22	1.60	1.90	1.57	4.91	5.59	3.08
<b>Ba</b>	1142	898	784	1297	1133	1299	1039
<b>La</b>	68.9	80.8	79.3	79.0	94.4	105	69.5
<b>Ce</b>	139	159	157	162	187	199	142
<b>Pr</b>	14.4	16.2	16.1	16.4	18.8	20.4	14.3
<b>Nd</b>	52.1	59.3	58.0	58.5	66.9	72.0	52.6
<b>Sm</b>	8.54	8.82	9.17	9.48	10.4	10.2	8.80
<b>Eu</b>	1.10	1.38	1.30	1.35	1.52	1.71	1.15
<b>Gd</b>	6.40	6.27	6.33	7.25	6.84	6.95	6.90
<b>Tb</b>	0.93	0.78	0.86	1.06	0.90	0.89	1.09
<b>Dy</b>	5.36	4.47	4.90	6.48	4.90	5.10	6.56

<b>Ho</b>	1.04	0.90	0.97	1.25	0.91	0.92	1.22
<b>Er</b>	2.89	2.48	2.67	3.49	2.47	2.66	3.68
<b>Tm</b>	0.42	0.40	0.40	0.52	0.38	0.41	0.52
<b>Yb</b>	2.89	2.37	2.53	3.26	2.44	2.53	3.47
<b>Lu</b>	0.42	0.37	0.39	0.50	0.36	0.39	0.51
<b>Hf</b>	5.58	5.84	5.49	6.16	5.74	6.29	5.83
<b>Ta</b>	0.90	0.71	0.71	0.85	0.73	0.78	1.02
<b>Pb</b>	7.78	2.59	2.73	4.03	6.40	9.99	5.53
<b>Th</b>	18.6	16.3	16.6	18.7	17.6	17.9	18.7
<b>U</b>	2.53	3.16	2.40	2.41	2.34	2.18	2.11

**Table 1: Continued**

<b>Sample no.</b>	<b>13MD03-4</b>	<b>13MD04-1</b>	<b>13MD04-2</b>	<b>13MD05-1</b>	<b>13MD06-1</b>	<b>13MD06-2</b>	<b>13MD07-1</b>
<b>Lithology</b>	<b>Rhyolite</b>	<b>Rhyolite</b>	<b>Rhyolite</b>	<b>Rhyolite</b>	<b>Rhyolite</b>	<b>Rhyolite</b>	<b>Rhyolite</b>
<b>Major element (wt.%)</b>							
<b>SiO<sub>2</sub></b>	75.3	76.1	75.6	77.7	75.4	76.1	78.8
<b>TiO<sub>2</sub></b>	0.18	0.17	0.18	0.15	0.18	0.17	0.09
<b>Al<sub>2</sub>O<sub>3</sub></b>	13.2	13.0	13.3	13.2	13.2	12.7	11.5
<b>TFe<sub>2</sub>O<sub>3</sub></b>	2.15	2.16	2.24	1.31	2.10	2.28	1.55
<b>MnO</b>	0.01	0.03	0.02	0.01	0.03	0.04	0.04
<b>MgO</b>	0.12	0.18	0.19	0.09	0.13	0.14	0.09
<b>CaO</b>	1.03	0.39	0.54	0.13	1.06	0.85	0.82
<b>Na<sub>2</sub>O</b>	2.31	1.81	2.32	2.73	2.17	2.34	2.03
<b>K<sub>2</sub>O</b>	5.65	6.14	5.52	4.65	5.74	5.30	5.09
<b>P<sub>2</sub>O<sub>5</sub></b>	0.04	0.03	0.06	0.03	0.04	0.04	0.04
<b>LOI</b>	1.74	1.23	1.32	1.29	1.72	1.68	1.44
<b>TOTAL</b>	99.9	99.8	99.8	99.9	99.8	99.8	100
<b>Trace element (ppm)</b>							
<b>Li</b>	9.85	7.08	10.9	19.5	9.63	7.83	12.2
<b>Be</b>	2.25	2.36	2.70	1.64	2.78	2.53	2.62
<b>Sc</b>	7.13	6.29	7.10	6.03	6.64	6.24	5.26
<b>V</b>	10.4	7.99	10.2	4.72	10.7	11.0	4.27
<b>Cr</b>	0.87	0.86	0.63	0.44	0.78	0.62	0.48
<b>Co</b>	0.43	0.50	0.69	0.32	0.63	0.53	0.26
<b>Ni</b>	1.23	1.31	1.35	1.20	1.35	1.38	1.41
<b>Cu</b>	2.00	0.61	1.68	3.09	1.41	0.89	0.49
<b>Zn</b>	33.2	33.7	39.9	32.0	41.4	37.1	38.6
<b>Ga</b>	17.6	17.4	18.3	16.7	17.9	16.8	17.5
<b>Rb</b>	159	159	148	125	153	137	149
<b>Sr</b>	53.5	43.9	65.6	33.4	81.6	67.6	55.0
<b>Y</b>	26.0	32.2	29.7	32.7	25.4	28.5	38.6
<b>Zr</b>	251	229	222	189	222	216	130
<b>Nb</b>	11.7	11.4	12.1	12.1	10.2	10.9	10.1
<b>Cs</b>	3.53	5.89	4.89	2.33	5.69	6.48	4.22

<b>Ba</b>	1232	1380	1347	865	1461	1235	252
<b>La</b>	93.7	83.1	94.3	71.6	91.3	96.1	50.5
<b>Ce</b>	181	174	182	143	181	185	94.0
<b>Pr</b>	18.7	17.3	18.5	15.7	18.0	19.0	12.2
<b>Nd</b>	65.7	60.3	65.5	57.4	63.1	67.9	47.9
<b>Sm</b>	9.98	9.51	10.2	9.95	9.39	10.2	9.66
<b>Eu</b>	1.53	1.45	1.63	1.27	1.57	1.56	0.64
<b>Gd</b>	6.78	6.79	7.12	7.27	6.53	7.30	7.90
<b>Tb</b>	0.90	0.95	0.96	1.03	0.86	0.97	1.20
<b>Dy</b>	5.04	5.99	5.51	6.49	4.91	5.60	6.96
<b>Ho</b>	0.92	1.18	1.06	1.24	0.92	1.05	1.23
<b>Er</b>	2.68	3.07	2.93	3.28	2.45	2.67	3.49
<b>Tm</b>	0.39	0.44	0.44	0.48	0.37	0.43	0.54
<b>Yb</b>	2.61	2.91	2.79	3.13	2.42	2.69	3.08
<b>Lu</b>	0.42	0.43	0.42	0.48	0.37	0.43	0.45
<b>Hf</b>	6.50	6.27	6.15	5.91	6.14	6.11	4.49
<b>Ta</b>	0.82	0.78	0.87	0.85	0.71	0.75	0.82
<b>Pb</b>	6.93	8.62	9.58	17.5	10.8	10.0	12.8
<b>Th</b>	17.4	17.2	17.9	18.6	17.0	17.7	17.1
<b>U</b>	2.29	2.27	2.09	2.91	2.44	2.16	2.47

Note:  $\text{TFe}_2\text{O}_3$  = Total iron measured as  $\text{Fe}_2\text{O}_3$ .

LOI = loss on ignition. Major elements are recalculated on anhydrous basis.



**Table 2. LA-ICP-MS zircon trace element data of Nuocang HSR samples**

Sample/spot #	Ti	Y	Nb	La	Ce	Pr	Nd	Sm	Eu	Gd	Tb	Dy
<b>Dark-CL cores: 30 spots</b>												
13MD02-1 01	3.33	6522	88.2	0.07	27.9	0.12	2.53	13.2	0.36	121	48.5	626
13MD02-1 03	2.98	5794	33.1	0.02	17.5	0.11	2.93	14.6	0.45	116	44.2	560
13MD02-1 06	2.20	4487	44.8	0.01	16.9	0.04	1.39	7.60	0.26	76.2	31.6	418
13MD03-1 01	2.64	4574	55.2	0.02	18.8	0.05	1.37	8.19	0.24	79.8	32.6	427
13MD03-1 04	4.91	5960	69.0	0.08	22.6	0.07	1.96	10.8	0.24	102	42.8	560
13MD03-1 05	3.02	6310	61.0	0.01	20.9	0.07	2.05	12.2	0.22	113	46.3	597
13MD03-1 06	4.12	6805	65.9	0.11	26.8	0.13	2.81	14.9	0.33	126	51.1	652
13MD03-1 12	2.92	2607	20.0	0.01	15.8	0.08	1.85	7.39	0.38	55.1	20.5	254
13MD03-1 13	2.03	4175	42.3	0.00	11.3	0.02	0.81	5.76	0.10	61.5	26.9	368
13MD03-1 16	3.13	3607	36.7	0.12	22.0	0.15	2.29	9.49	0.45	76.3	28.8	355
13MD03-1 17	2.82	7095	41.6	0.01	18.7	0.11	2.85	15.0	0.36	132	53.7	681
13MD03-1 18	2.88	4877	75.7	0.01	21.2	0.07	1.56	8.91	0.20	87.0	35.4	455
13MD03-1 19	5.57	5096	30.4	0.22	17.2	0.18	2.83	13.8	0.48	108	40.6	508
13MD04-1 01	2.66	7117	69.5	0.01	26.1	0.10	2.55	15.3	0.38	138	53.0	678
13MD04-1 02	4.11	3251	27.3	0.06	9.83	0.04	0.70	5.05	0.17	50.3	20.9	283
13MD04-1 03	3.01	4400	37.1	0.03	13.2	0.04	1.37	6.61	0.18	70.9	29.5	400
13MD06-2 03	4.34	3875	54.7	0.20	16.8	0.10	1.51	6.78	0.17	66.3	27.4	361
13MD06-2 08	2.85	4516	63.8	0.00	16.6	0.04	1.02	7.10	0.13	72.9	31.0	421
13MD06-2 09	2.63	6001	88.9	0.02	26.1	0.07	2.01	11.2	0.47	108	43.6	562
13MD06-2 11	3.25	4386	50.8	0.06	22.5	0.10	1.79	9.24	0.35	84.3	33.3	424
13MD06-2 12	3.30	5123	60.2	0.01	18.9	0.05	1.22	8.92	0.22	86.9	36.7	475
13MD07-1 03	2.17	6897	51.9	0.03	22.0	0.12	2.84	15.5	0.41	129	51.2	660
13MD07-1 06	2.61	5922	78.3	0.01	26.7	0.07	1.93	11.0	0.28	107	43.0	561
13MD07-1 07	1.79	6645	48.9	0.01	17.3	0.08	2.29	13.1	0.17	118	47.5	616
13MD07-1 08	1.86	5972	76.4	0.03	24.3	0.09	1.97	10.6	0.23	104	43.2	564
13MD07-1 09	3.81	6178	101	0.17	26.3	0.13	2.00	10.8	0.21	103	43.3	575
13MD07-1 18	2.16	4521	38.2	0.01	12.2	0.03	0.99	6.80	0.13	68.8	29.7	401
13MD07-1 20	2.53	6157	32.2	0.03	14.2	0.10	2.46	12.9	0.27	113	44.9	579
13MD07-1 21	3.41	4592	51.1	0.01	25.2	0.09	2.20	11.0	0.44	97.8	36.8	453
13MD07-1 22	2.49	4434	39.3	0.00	13.2	0.03	1.00	6.72	0.17	67.5	29.5	398
<b>Light-CL rims: 13 spots</b>												
13MD03-1 08	2.70	1050	5.64	0.02	9.01	0.06	1.25	3.62	0.24	23.7	8.10	98.0
13MD03-1 11	4.38	1084	4.10	0.00	14.5	0.08	2.16	5.03	0.42	27.5	8.95	105
13MD03-1 14	3.20	1109	5.69	0.03	10.9	0.05	1.30	3.69	0.20	24.7	8.58	103
13MD03-1 15	3.48	1246	5.72	0.00	10.6	0.07	1.47	4.61	0.21	30.1	9.84	118
13MD03-1 20	4.05	1081	4.41	0.01	13.6	0.09	1.80	4.50	0.40	26.0	8.75	103
13MD04-1 04	3.91	964	3.96	0.00	10.7	0.05	1.27	3.53	0.28	21.7	7.39	89.0
13MD06-2 04	3.38	1071	4.58	0.01	12.1	0.06	1.64	4.41	0.30	25.5	8.48	102
13MD07-1 02	3.12	1041	4.92	0.02	10.3	0.04	1.09	3.51	0.21	23.1	7.95	98.8
13MD07-1 04	2.91	1007	4.32	0.00	10.8	0.05	1.25	3.71	0.25	22.4	7.78	93.6
13MD07-1 05	2.72	1128	5.51	0.01	10.2	0.05	1.09	3.72	0.20	24.2	8.58	104

13MD07-1 12	3.66	994	4.93	0.01	9.38	0.04	0.94	3.49	0.17	22.1	7.69	92.8
13MD07-1 14	3.18	1018	5.20	0.04	9.16	0.06	0.89	3.25	0.19	22.7	7.76	94.9
13MD07-1 17	3.44	1818	9.03	0.05	13.3	0.09	1.84	6.34	0.24	41.5	14.3	173

**Light-CL grains: 11 spots**

13MD02-1 04	4.54	1476	2.10	0.01	12.6	0.20	4.78	9.62	0.85	44.4	13.2	147
13MD02-1 05	11.2	535	0.98	0.01	6.06	0.12	2.09	3.85	0.52	16.9	4.89	53.2
13MD02-1 07	8.51	892	0.93	0.02	7.24	0.22	4.06	6.81	1.17	29.4	8.52	90.6
13MD02-1 08	8.00	464	1.06	0.01	5.98	0.09	1.51	2.78	0.37	12.6	3.93	44.1
13MD06-2 01	5.81	809	2.83	0.01	12.0	0.05	1.68	4.01	0.36	21.7	6.99	77.2
13MD06-2 02	8.50	729	1.74	0.02	14.3	0.17	2.86	5.24	0.71	22.9	6.51	72.5
13MD06-2 06	4.93	732	2.58	0.01	11.4	0.06	1.56	3.04	0.27	18.5	5.99	70.0
13MD07-1 10	4.75	727	2.78	0.11	9.58	0.07	1.19	3.16	0.27	17.6	5.93	70.4
13MD07-1 11	4.27	1246	5.46	0.01	13.6	0.09	1.80	5.04	0.35	29.3	9.75	117
13MD07-1 13	2.82	1050	4.80	0.08	9.75	0.07	1.25	3.56	0.23	22.7	7.83	95.5
13MD07-1 15	2.87	1323	5.72	0.01	12.5	0.09	1.94	5.51	0.32	32.0	10.8	125

**Table 2. Continued:**

Sample/spot #	Ho	Er	Tm	Yb	Lu	Hf	Ta	Th	U	$T_{\text{TiZ}}$ (°C)	Eu/Eu*
<b>Dark-CL cores: 30 spots</b>											
13MD02-1 01	238	1010	204	1787	303	14316	18.3	2148	3758	693	0.03
13MD02-1 03	213	898	177	1538	259	13488	8.72	1303	2410	684	0.03
13MD02-1 06	161	706	143	1255	214	13495	11.4	1506	2650	660	0.03
13MD03-1 01	167	733	148	1283	227	13606	13.3	1252	2675	674	0.03
13MD03-1 04	218	944	189	1621	281	14198	15.4	2289	3679	727	0.02
13MD03-1 05	235	997	202	1737	294	15503	14.8	1700	3276	685	0.02
13MD03-1 06	250	1067	212	1834	313	14222	15.6	1934	3503	712	0.02
13MD03-1 12	95.5	403	81.4	727	127	12331	6.05	685	1117	682	0.06
13MD03-1 13	148	666	137	1219	219	15069	11.2	1147	2587	654	0.02
13MD03-1 16	133	557	111	955	166	12880	10.1	1634	2097	688	0.05
13MD03-1 17	262	1110	220	1889	330	14757	9.83	1818	3045	680	0.03
13MD03-1 18	177	762	152	1293	231	15842	22.4	2218	3619	681	0.02
13MD03-1 19	192	805	159	1356	239	13363	7.27	1113	1943	739	0.04
13MD04-1 01	262	1116	218	1875	331	14602	15.7	1955	3389	675	0.02
13MD04-1 02	116	523	106	936	172	14077	8.06	698	1644	712	0.03
13MD04-1 03	160	708	141	1250	225	13588	9.20	1142	2304	685	0.02
13MD06-2 03	141	626	128	1136	202	14868	14.6	897	2175	716	0.03
13MD06-2 08	168	730	149	1307	232	15280	17.1	1270	2923	680	0.02
13MD06-2 09	218	947	192	1713	297	15128	18.9	1650	3326	674	0.04
13MD06-2 11	163	687	137	1163	207	13700	14.4	1558	2487	691	0.04
13MD06-2 12	188	811	162	1397	252	14892	15.1	2084	3374	693	0.02
13MD07-1 03	252	1066	210	1794	314	14314	12.3	1778	3025	659	0.03
13MD07-1 06	215	915	182	1538	271	14660	20.2	2549	3799	673	0.02
13MD07-1 07	242	1048	207	1758	312	15432	12.3	1822	3225	644	0.01
13MD07-1 08	216	944	188	1592	284	15338	19.1	2162	3589	647	0.02
13MD07-1 09	226	982	199	1722	307	15572	22.3	1718	3688	705	0.02
13MD07-1 18	161	714	146	1276	229	14681	10.7	1412	2805	658	0.02

13MD07-1 20	224	971	194	1658	293	14735	8.37	1422	2497	671	0.02
13MD07-1 21	168	707	140	1186	210	13218	13.3	2258	2728	695	0.04
13MD07-1 22	160	714	145	1276	229	13797	9.69	1199	2389	670	0.02
<b>Light-CL rims: 13 spots</b>											
13MD03-1 08	37.8	168	35.7	325	61.7	11472	2.05	146	285	676	0.08
13MD03-1 11	39.1	170	35.0	324	61.1	10746	1.44	190	274	717	0.11
13MD03-1 14	40.1	174	36.4	330	63.1	12107	2.00	198	332	690	0.06
13MD03-1 15	45.5	195	40.4	366	69.1	11574	1.94	193	324	697	0.05
13MD03-1 20	40.0	170	35.2	324	63.0	11202	1.54	198	296	710	0.11
13MD04-1 04	34.1	150	30.8	293	56.2	11354	1.53	163	272	707	0.10
13MD06-2 04	38.5	168	35.1	331	61.7	11529	1.77	205	327	695	0.09
13MD07-1 02	37.4	165	34.5	314	59.5	11986	1.83	176	302	688	0.07
13MD07-1 04	35.9	158	32.6	299	57.8	11440	1.63	181	297	682	0.08
13MD07-1 05	40.4	176	36.4	331	63.0	11918	1.99	203	339	676	0.06
13MD07-1 12	36.0	157	32.7	295	57.3	11932	1.82	170	298	702	0.06
13MD07-1 14	36.3	162	33.5	300	58.8	12101	1.84	171	292	690	0.07
13MD07-1 17	64.8	281	57.4	505	94.2	12192	2.93	318	497	696	0.05
<b>Light-CL grains: 11 spots</b>											
13MD02-1 04	53.4	225	45.3	418	75.2	10260	0.93	163	203	720	0.13
13MD02-1 05	19.1	81.2	16.9	161	30.0	8571	0.38	57.2	73.4	808	0.20
13MD02-1 07	32.0	134	27.3	252	46.8	8726	0.40	75.5	96.3	780	0.25
13MD02-1 08	16.3	71.3	15.3	143	27.6	9322	0.40	47.9	73.0	774	0.19
13MD06-2 01	29.7	126	26.7	248	47.3	10982	1.02	120	188	743	0.12
13MD06-2 02	26.2	113	23.4	222	43.2	9288	0.76	103	128	780	0.20
13MD06-2 06	26.0	113	23.7	218	43.2	10693	1.09	101	161	728	0.11
13MD07-1 10	26.1	114	24.0	217	43.0	11151	0.99	98.4	161	724	0.11
13MD07-1 11	44.3	196	40.1	363	69.7	11398	1.85	250	355	715	0.09
13MD07-1 13	37.1	168	34.8	317	63.0	11736	1.93	160	267	680	0.08
13MD07-1 15	47.4	206	42.0	379	73.5	11157	1.93	273	375	681	0.07

**Table 3. Quartz Ti content and geothermometer calculation results**

<b>Spot size: 50 <math>\mu\text{m}</math>; Fluence: 10 J/cm<sup>2</sup>; Rep Rate: 10 Hz</b>			
<b>Sample /Spot #</b>	<b><sup>48</sup>Ti (ppm)</b>	<b>DC/LR/M</b>	<b>T (<math>\alpha_{\text{TiO}_2}=0.6</math>, °C)</b>
13MD02-4-1 01	18.1	DC	621
13MD02-4-1 02	19.7	DC	629
13MD02-4-1 03	37.1	LR	693
13MD02-4-1 04	41.3	LR	704
13MD02-4-1 05	40.6	DC	702
13MD02-4-1 06	176	DC	895
13MD02-4-1 07	35.2	LR	687
13MD02-4-1 08	70.4	LR	767
13MD05-1-1 01	82.8	LR	788
13MD05-1-1 02	40.4	M	702
13MD05-1-1 03	38.5	M	697
13MD05-1-1 04	33.9	DC	683
13MD05-1-1 05	19.9	DC	630
13MD05-1-1 06	56.7	LR	738
13MD05-1-1 07	53.4	LR	694
13MD05-1-1 08	39.7	M	700
13MD05-1-1 09	37.5	M	733
13MD05-1-1 10	55.4	DC	740
13MD06-2-1 01	33.4		681
13MD06-2-1 02	55.4	/	738
13MD06-2-1 03	45.8		716
13MD06-2-1 04	41.8		706
13MD06-2-2 01	18.8	DC	625
13MD06-2-2 02	33.4	LR	681
13MD06-2-2 03	33.4	LR	682
13MD06-2-2 04	39.9	LR	701
13MD06-2-2 05	24.9	DC	652
13MD06-2-2 06	57.9	LR	743
13MD06-2-2 07	28.1	DC	664
13MD06-2-2 08	21.0	DC	635
13MD06-2-2 09	101	/	814
13MD06-2-2 10	39.3	LR	699
13MD06-2-3 01	19.5	DC	628
13MD06-2-3 02	74.0	LR	773
13MD06-2-3 03	25.5	DC	654
13MD06-2-3 04	90.5	M	799
13MD06-2-3 05	71.9	LR	769
13MD06-2-3 06	19.1	DC	626
13MD06-2-3 07	36.7	M	691
13MD06-2-3 08	78.4	LR	780
13MD06-2-3 09	83.2	LR	788
13MD06-2-3 10	80.7	LR	784

13MD07-1-1 01	17.4	DC	618
13MD07-1-1 02	79.1	DC	782
13MD07-1-1 03	35.7	M	689
13MD07-1-1 04	64.8	LR	757
13MD07-1-1 05	28.1	DC	664
13MD07-1-1 06	32.6	DC	679
13MD07-1-1 07	140	M	860
13MD07-1-1 08	141	LR	862
<b>Spot size: 75 <math>\mu</math>m; Fluence: 8 J/cm<sup>2</sup>; Rep Rate: 8 Hz</b>			
<b>Sample/Spot</b>	<b><sup>49</sup>Ti (ppm)</b>	<b>DC/LR/M</b>	<b>T (<math>\alpha_{\text{TiO}_2}</math>=0.6, °C)</b>
13MD02-4-1 01	118	DC	836
13MD02-4-1 02	62.7	LR	753
13MD02-4-1 03	567	LR	1114
13MD02-4-1 04	161	DC	881
13MD02-4-2 01	21.6		638
13MD02-4-2 02	53.3	/	733
13MD02-4-2 03	59.4		746
13MD02-4-2 04	25.7		655
13MD05-1-1 01	111	LR	827
13MD05-1-1 02	58.8	LR	745
13MD05-1-1 03	52.8	LR	732
13MD05-1-1 04	35.4	DC	688
13MD05-1-1 05	26.2	DC	657
13MD07-1-1 01	195	DC	911
13MD07-1-1 02	77.5	M	779
13MD07-1-1 03	74.2	LR	774
13MD07-1-1 04	129	LR	849
13MD07-1-2 01	21.1	DC	636
13MD07-1-2 02	43.3	M	709
13MD07-1-2 03	41.8	LR	706
13MD07-1-2 04	116	M	833
13MD07-1-2 05	22.4	DC	641
13MD07-1-2 06	232	DC	941
13MD07-1-2 07	162	DC	883
13MD07-1-2 08	129	LR	848
13MD07-1-2 09	114	LR	830
13MD07-1-2 10	79.0	LR	782